Direct synthesis of 2,5-furandicarboxylic acid from biomass-derived fructose using multifunctional Pd-Ru nanoparticles supported mesoporous organic polymers functionalized with sulfonic acid

Pillaiyar Puthiaraj , Jongmin Park , Yuyeol Choi , Woosung Leem , Kyungsu Na [*]

Department of Chemistry, Chonnam National University, Gwangju 61186, Republic of Korea

ARTICLE INFO

ABSTRACT

The sustainable production of 2,5-furan dicarboxylic acid (FDCA) from biomass-derived fructose is crucial yet challenging for developing high-yield renewable alternatives to fossil-based polymers. Herein, a sulfonic acid-functionalized cross-linked porous organic polymer (S-CPOP) was synthesized via a facile Friedel–Crafts reaction, offering a high surface area (1050 m^2 g^{-1}), mesoporosity, and abundant Brønsted acid sites (1.33 mmol g^{-1}). The S-CPOP was employed both as a solid acid catalyst for fructose dehydration and as a support for monometallic (Pd and Ru) and bimetallic (Pd-Ru) nanoparticles (NPs) for subsequent oxidation processes. The Pd-Ru/S-CPOP exhibited outstanding catalytic performance in the direct, one-pot conversion of fructose to FDCA under base-free conditions, achieving a remarkably high FDCA yield of 95 % within a short reaction time. This exceptional activity is attributed to the synergistic effect between Pd and Ru NPs, the abundant sulfonic acid groups, and the mesoporous structure of the S-CPOP, which facilitates efficient mass transfer and reactant accessibility. The radical quenching, kinetic and thermodynamic experiments were also systematically evaluated, revealing key insights into the reaction mechanism. Notably, the catalyst demonstrated excellent stability and recyclability, retaining high activity over five consecutive runs without significant metal leaching or structural degradation. This work presents a cost-effective, environmentally benign, and multifunctional catalytic system for efficient FDCA production, offering a promising route for sustainable polymer precursor synthesis in bio-based industries.

1. Introduction

The conversion of biomass into high-value-added chemicals, including alternative fuels and fine chemicals, has emerged as a focal point in the sustainable chemical industry, driven by the rapid global depletion of fossil fuels and associated environmental concerns [1,2]. Among the various platform chemicals derived from biomass, 5-hydroxymethylfurfural (HMF) is particularly noteworthy, as it can be synthesized through the selective dehydration of C6 carbohydrate-based biomass, such as D-fructose and D-glucose [3]. HMF represents a versatile precursor to a wide array of value-added chemicals. Of these, its oxidized derivative, 2,5-furandicarboxylic acid (FDCA), garnered significant attention due to its versatile applications in the synthesis of high-performance polymers such as nylons, polyesters, polyamides, and plasticizers [4,5]. Notably, FDCA-based polyethylene furanoate has emerged as a promising, sustainable alternative to traditional

terephthalate-based polymer plastics, such as polybutylene terephthalate (PBT) and polyethylene terephthalate (PET), exhibiting superior properties relative to these conventional plastics, including improved thermal and mechanical performance, as well as enhanced barrier properties [6]. Therefore, the development of efficient and environmentally benign catalytic systems for FDCA production from biomass-derived feedstocks is attracting considerable attention.

Biomass conversion to HMF has mainly been achieved using homogeneous and/or solid acid catalysts [7]. However, homogeneous catalysts present challenges due to handling difficulties, corrosive nature, environmental pollution, complex product separation, and limited reusability in subsequent reactions [8,9]. To mitigate these issues, research has increasingly focused on heterogeneous porous catalysts for biomass conversion to HMF, due to their ease of separation from the reaction mixture and facile recyclability. Examples of such catalysts include phosphorus- and SO_3H-functionalized carbon materials


[10–12], SO$_3$H-functionalized metal-organic frameworks [13], *k*-carra-geenan/MIL-101(Cr) [14], SO$_3$H-functionalized alumina [15], metal carbides [16], ionic liquid-supported metal oxides [17,18], dendritic mesoporous silica particles [19], SiNP-SO$_3$H-C$_{16}$ [20], Fe$_3$O$_4$@SBA-16-SO$_3$H [21], AgFe$_2$O$_4$/SBA-16/SO$_3$H [22], KIT-6-PrSO$_3$H [23], Sn(IV)/amine-functionalized γ-Al$_2$O$_3$ [24], and AgFe$_2$O$_4$/TiO$_2$-SO$_3$H [25]. Despite progress, some catalysts still exhibit low HMF yields, and their preparation often involves multiple steps. Furthermore, sulfonic acid-functionalized solid catalysts often require the use of hazardous sulfonating agents, such as ClSO$_3$H and/or H$_2$SO$_4$, during their synthesis, raising challenges related to safety, environmental impact, and chemical instability, which can ultimately limit catalyst reusability. This highlights the urgent necessity to develop efficient, environmentally friendly, and stable catalysts that are easy to prepare, handle safely, and are capable of effectively catalyzing biomass dehydration to HMF.

Likewise, several solid noble metal catalytic materials have been investigated for the aerobic oxidation of HMF to FDCA, including Au [26,27], Pd [28], Pt [29,30], and Ru [31–34], as well as their bimetallic nanoparticles (NPs) [35–37], which are generally supported by various materials such as carbon [30,31,33,36], resin [29], hydrotalcite [26,35], layered double hydroxide [37], and metal oxides [27,32,34]. Despite these advancements, several challenges persist, particularly in achieving high FDCA yields with certain catalysts, the requirement for base additives, prolonged reaction times (ranging from 12 to 24 h), and the high cost of Au and Pt NPs. Additionally, issues related to catalyst stability and reusability further hinder the practical application of these systems. Therefore, developing a stable, economically viable catalyst for HMF conversion to FDCA without requiring base additives remains a significant challenge in this field.

Porous organic polymers (POPs) have recently gained more attention due to their ease of synthesis from inexpensive precursors, high surface areas, tunable pore sizes, customizable chemical functionalities, and excellent chemical/thermal stability [38,39]. These desirable features make POPs promising candidates for diverse applications, such as catalysis, gas/energy storage, and environmental remediation [39–41].

Recent studies have demonstrated the use of phosphate-functionalized POPs in biomass conversion to HMF, achieving an 85 % yield and a turnover frequency (TOF) of 18.9 h^{-1} at 120 °C [42]. Similarly, Ru NPs supported on a covalent triazine framework have been employed as a catalyst for HMF oxidation, achieving a 77.6 % yield of FDCA with a TOF of 13.3 h^{-1} at 140 °C with 20 bar of air [43]. Few researchers have explored the one-pot synthesis of FDCA from fructose utilizing a sequential catalytic approach [44–51]. In this process, one catalyst facilitates the conversion of fructose to HMF, while another catalyst is employed for the subsequent oxidation of HMF to FDCA. Until now, as far as we know, there are no reports on using POPs directly functionalized with sulfonic acid groups as a single catalyst for the biomass conversion to HMF and its subsequent oxidation to FDCA. Therefore, the development of such multifunctional catalysts could significantly enhance the efficiency and economic viability of these reactions while simultaneously reducing both manpower and chemical waste during the reaction/purification process, thereby advancing the shift toward a bio-based sustainable chemical industry.

Herein, we synthesized a sulfonic acid-functionalized cross-linked POP with a high surface area and mesoporous structure using inexpensive, commercially available precursors through a simple Friedel–Crafts reaction (step I in Scheme 1). The catalytic performance of this solid acid catalyst was initially evaluated in the dehydration of fructose, achieving an excellent HMF yield with a TOF of 38.0 h^{-1}. Building on this, the S-CPOP was utilized as a support for incorporating monometallic Pd and Ru (Pd/S-CPOP and Ru/S-CPOP), as well as the bimetallic Pd-Ru (Pd-Ru/S-CPOP) NPs (step II in Scheme 1). Notably, the Pd-Ru/S-CPOP catalyst exhibited exceptional activity in the aerobic oxidation of HMF under base-free conditions, achieving complete conversion and a 98 % yield of FDCA with a TOF of 30.1 h^{-1}. This superior catalytic performance can be attributed to the mesoporous structure of S-CPOP, which facilitates efficient reactant transport during the reaction. Finally, the Pd-Ru/S-CPOP catalyst was successfully employed in the direct conversion of fructose to FDCA using O$_2$ as the oxidant under base-free conditions. The catalyst demonstrated excellent recyclability, with
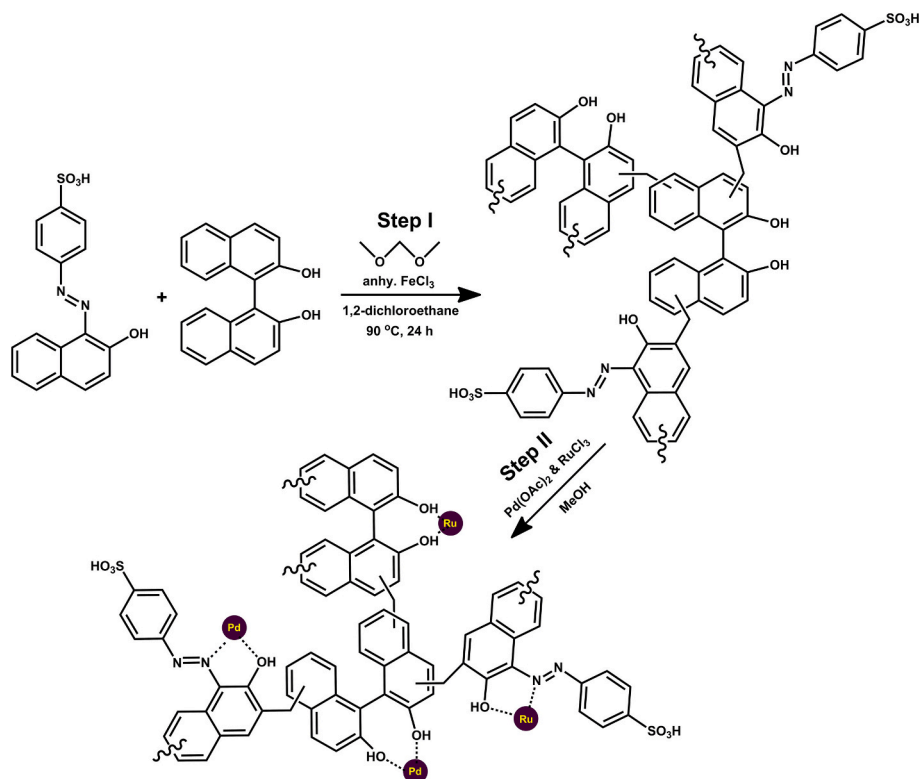
Scheme 1. Synthesis of S-CPOP (step I) and subsequent metallation of Pd and Ru NPs as monometallic NPs or bimetallic NPs (step II).

easy separation from the reaction mixture, maintaining its high activity over five runs. The simplicity of its synthesis and its renewability make this catalytic process both environmentally friendly and economically viable for the sustainable production of FDCA from biomass-derived fructose.

2. Experimental sections

2.1. Chemicals

Dimethoxymethane (99 %, Sigma–Aldrich), 1,1′-bi-2-naphthol (>99 %, Tokyo Chemical Industry Co., Ltd.; TCI), 4-(2-hydroxy-1-naphthylazo)benzenesulfonic acid (HNBSA; >97 %, TCI), anhydrous iron(III) chloride (FeCl$_3$; >97 %, DAEJUNG), D-(−)-fructose (>99 %, TCI), ruthenium(III) chloride (RuCl$_3$; >99 %, Sigma–Aldrich), palladium(II) acetate (Pd(OAc)$_2$; 97 %, Sigma–Aldrich), sodium borohydride (>98 %, Sigma–Aldrich), 5-hydroxymethylfurfural (HMF; 99 %, Sigma–Aldrich), and dimethyl sulfoxide-d_6 (DMSO-d_6, 99.9 % atom D%, Sigma–Aldrich) were purchased and utilized directly without further purification. All the solvents (high-performance liquid chromatography; HPLC grade) involved in this study were received from DAEJUNG chemicals and metals (South Korea). O$_2$ (99.99 %) gas was obtained from Hankook Special Gas Co., Ltd. (South Korea).

2.2. Catalysts synthesis

2.2.1. Synthesis of S-CPOP

The S-CPOP was synthesized through a facile route of Friedel–Crafts electrophilic substitution reaction between 1,1′-bi-2-naphthol and HNBSA using dimethoxymethane cross-linker, as outlined in step I in Scheme 1. In the synthesis, dimethoxymethane (1.06 mL), 1,1′-bi-2-naphthol (0.57 g), HNBSA (0.7 g), and 1,2-dichloroethane (DCE; 120 mL) were added to a round-bottom flask and stirred at room temperature (RT) for 30 min. Anhydrous FeCl$_3$ (2.00 g) was introduced, and the reaction flask was equipped with a condenser and stirred at 50 °C overnight. After heating at 90 °C for 24 h, the brown solid was collected by filtration and washed sequentially with copious amounts of *N*,*N*-dimethylformamide (DMF), ethanol, and water. The final solid was further purified by Soxhlet extraction using DMF:ethanol (100/100 mL) mixture for 48 h, followed by drying under reduced pressure at 160 °C overnight to obtain S-CPOP.

2.2.2. Synthesis of Pd NPs supported on S-CPOP (Pd/S-CPOP)

As schematized in step II in Scheme 1, pre-synthesized Pd(OAc)$_2$ (30 mg) and S-CPOP (500 mg) with the mass ratio of 6:100 were added to methanol (50 mL) and stirred vigorously at RT overnight. Then, methanol was evaporated under reduced pressure to obtain the Pd(II)/S-CPOP composite material. This composite was dispersed in water (50 mL), and then an aqueous solution of NaBH$_4$ (0.5 mL, 0.1 M) was added dropwise with constant stirring for 10 min. The solid product was collected by filtration, washed with copious amounts of water and methanol to remove the unbound Pd particles, and dried at 160 °C under reduced pressure overnight to obtain Pd/S-CPOP.

2.2.3. Syntheses of Ru NPs and Pd-Ru bimetallic NPs supported on S-CPOP (Ru/S-CPOP and Pd-Ru/S-CPOP)

Ru/S-CPOP and Pd-Ru/S-CPOP catalysts with varying Pd-to-Ru mass ratios were synthesized via the same procedure as Pd/S-CPOP, using alternative metal precursors instead Pd(OAc)$_2$. For Ru/S-CPOP, 30 mg of RuCl$_3$ was used, corresponding to a RuCl$_3$:S-CPOP mass ratio of 6:100. Bimetallic catalysts were prepared by co-impregnating Pd(OAc)$_2$ and RuCl$_3$ in different ratios: 15 mg of each metal precursors (Pd(OAc)$_2$: RuCl$_3$:S-CPOP = 3:3:100) for Pd-Ru/S-CPOP; 7.5 mg of Pd(OAc)$_2$ and 22.5 mg of RuCl$_3$ (1.5:4.5:100) for Pd$_{0.5}$-Ru$_{1.5}$/S-CPOP; and 22.5 mg of Pd(OAc)$_2$ with 7.5 mg of RuCl$_3$ (4.5:1.5:100) for Pd$_{1.5}$-Ru$_{0.5}$/S-CPOP were used.

2.3. Catalysts characterization

High-performance X-ray photoelectron spectroscopy (XPS) was performed using a hemispherical analyzer (Thermo Scientific, USA) with a monochromatic Al Kα X-ray source. Fourier transform-infrared (FT-IR) spectra were collected using a Nicolet iS50R spectrometer, covering a wavelength range of 4000–650 cm^{-1}. The FT-IR spectrum of pyridine-adsorbed S-CPOP was recorded to estimate the acid strength of the polymer. Before analysis, the polymer was exposed to pyridine vapor at room temperature for one day. The C, H, N, and S contents of the S-CPOP were analyzed with a Vario MICRO cube elemental analyzer. Powder X-ray diffraction (XRD) was performed with a Rigaku MiniFlex 600 instrument with a Cu Kα radiation (λ = 1.5405 Å) with a 2θ range of 5–90°. N$_2$ sorption isotherm analysis was measured at 77 K using a BELSORP MAX II volumetric analyzer. The specific surface area and pore size were estimated using Brunauer–Emmett–Teller (BET) theory and the non-local density functional theory (NLDFT) model with a slit pore geometry, based on the adsorption isotherm, respectively. Before N$_2$ sorption analysis, the catalytic materials were vacuum-treated at 160 °C for 3 h. Field emission scanning electron microscopy (FESEM) with energy-dispersive spectroscopy (EDS) images were obtained using a GeminiSEM 500. Field emission transmission electron microscope (FETEM) and scanning TEM (STEM) with EDS were performed using a JEM-2100F electron microscope. STEM-EDS imaging used high-angle annular dark field (HAADF) modes. The Pd and Ru contents were determined by inductively coupled plasma-optical emission spectroscopy (ICP–OES) using an OPTIMA 8500 (PerkinElmer Inc.). Nuclear magnetic resonance (NMR) spectra were recorded using an Agilent-ProPulse 500 MHz spectrometer.

2.4. Reaction studies

2.4.1. Dehydration of fructose to HMF

Typically, fructose (2 mmol) and the desired catalyst (20–80 mg) were added to a 20 mL batch reactor autoclave containing 5 mL of solvent. The reaction mixture was heated to 110–130 °C with a stirring speed of 400 rpm for the desired reaction time. After the reaction, the reactor was cooled to RT, the mixture was diluted with the respective solvent to a final volume of 30 mL, then centrifuged at 10,000 rpm for 10 min to separate the catalyst. The collected catalyst was washed three times with 10 mL of methanol to remove other impurities and reused in subsequent runs. The supernatant was filtered again through a 0.22 μm syringe filter before high-performance liquid chromatography (HPLC) analysis.

2.4.2. Aerobic oxidation of HMF to FDCA

Typically, HMF (2 mmol) and the desired catalyst (20–60 mg) were added to a 20 mL batch reactor autoclave containing 5 mL of DMSO: water (*v*/v; 3:2) mixture. The autoclave was then pressurized with 10 bar of O$_2$ gas at RT and heated to 110–130 °C with a stirring speed of 400 rpm for the desired reaction time. The catalyst separation procedure was carried out in the same manner as in the fructose dehydration reaction process.

2.4.3. Direct conversion of fructose to FDCA

Typically, fructose (2 mmol) and the desired catalyst (60 mg) were added to a 20 mL batch reactor autoclave containing 5 mL of DMSO: water (*v*/v; 3:2) mixture. The reaction mixture was heated to 130 °C with a stirring speed of 400 rpm for 1 h. The reactor was then cooled to RT, and the autoclave was pressurized with 10 bar of O$_2$ gas at RT, then heated to 130 °C for the remaining reaction time. The reaction was quenched by placing the reactor in an ice bath, followed by depressurization. The catalyst separation procedure was carried out in the same manner as in the fructose dehydration reaction process.

2.4.4. Product analysis

The quantitative analysis of the reaction mixture was carried out using HPLC (Perkin Elmer series 200) equipped with both a refractive index (RI) and an ultraviolet (UV) detector. The compounds in the reaction mixture were separated at 60 °C using 5 mM H_2SO_4 as the mobile phase (flow rate: 0.6 mL min^{-1}) on an Aminex Bio-Rad HPX-87H column (300 × 7.8 mm). Fructose, levulinic acid (LA), and formic acid (FA) were analyzed using the RI detector, while HMF, 2,5-diformylfuran (DFF), and 5-formyl-2-furancarboxylic acid (FFCA) were quantified with the UV detector at an absorption wavelength of 285 nm. FDCA was analyzed at an absorption wavelength of 260 nm. The concentrations of the compounds were determined using calibration curves constructed with commercial standards. The fructose conversion (Eq. (1)), HMF yield (Eq. (2)), HMF selectivity (Eq. (3)), TOF of the catalyst (Eq. (4)), and carbon balance (CB; Eq. (5)) in the dehydration reaction were calculated using the following equations [23,52].

$$\text{Fructose conversion (\%)} = 1 - \frac{\text{moles of unreacted fructose}}{\text{moles of initial fructose}} \times 100 \tag{1}$$

$$\text{HMF yield (\%)} = \frac{\text{moles of produced HMF}}{\text{moles of initial fructose}} \times 100 \tag{2}$$

$$\text{HMF selectivity (\%)} = \frac{\text{moles of produced HMF}}{\text{moles of converted fructose}} \times 100 \tag{3}$$

$$\text{TOF } (h^{-1}) = \frac{\text{moles of HMF formed}}{\text{moles of active sulfonic acid sites} \times \text{reaction time}} \tag{4}$$

$$\text{CB (\%)} = \frac{\sum (\text{moles of products formed} + \text{moles of unreacted reactant})}{\text{moles of initial reactant}} \times 100 \tag{5}$$

Similarly, the HMF conversion (Eq. (6)), the yield of DFF, FFCA, and FDCA (Eq. (7)), FDCA selectivity (Eq. (8)), and the TOF of the catalyst (Eq. (9)) in the aerobic oxidation reaction were calculated using the following equations [31].

$$\text{HMF conversion (\%)} = 1 - \frac{\text{moles of unreacted HMF}}{\text{moles of initial HMF}} \times 100 \tag{6}$$

$$\text{Yield of A (\%)} = \frac{\text{moles of produced A}}{\text{moles of initial HMF}} \times 100 \tag{7}$$

where A = DFF, FFCA, and FDCA

$$\text{FDCA selectivity (\%)} = \frac{\text{Yield of FDCA}}{\text{Conversion of HMF}} \times 100 \tag{8}$$

$$\text{TOF } (h^{-1}) = \frac{\text{moles of FDCA formed}}{\text{moles of active Pd\&Ru sites} \times \text{reaction time}} \tag{9}$$

3. Results and discussions

3.1. Materials characterization

The chemical functionalities, porous characteristics, and morphology of the synthesized S-CPOP were confirmed through several
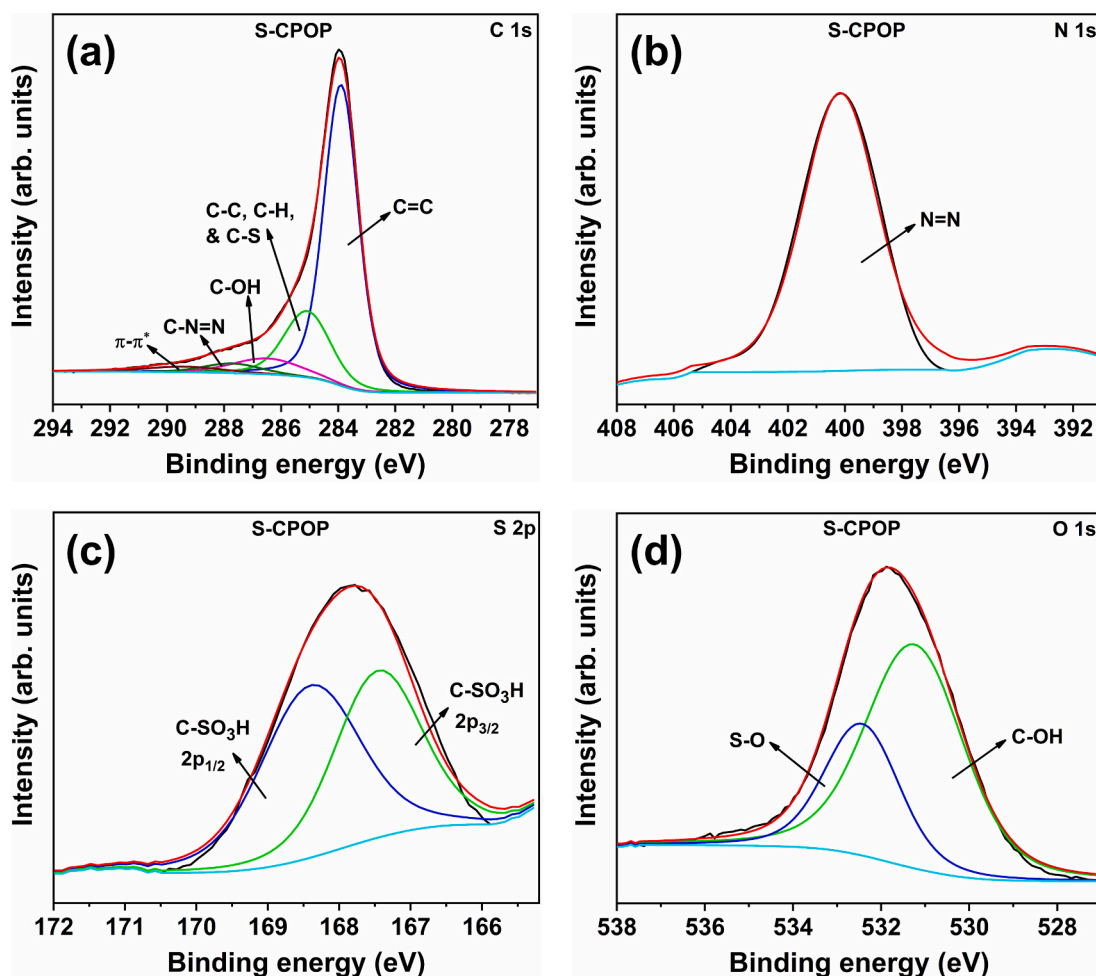

Fig. 1. Deconvoluted XPS of (a) C 1s, (b) N 1s, (c) S 2p, and (d) O 1s core levels of the S-CPOP catalyst.

analytical techniques. The chemical functionalities and elemental states of S-CPOP were first analyzed using XPS (Fig. 1). The deconvoluted C 1 s spectrum of S-CPOP (Fig. 1(a)) exhibited five binding energy peaks at 283.9, 285.1, 286.5, 287.8, and 289.8 eV, assigning to C=C, C–C/C–H/ C–S, C–OH, C-N=N, and π–π^* transitions, respectively [39]. The N 1 s peak (Fig. 1(b)) of the azo bond was detected at 400.2 eV [53]. The deconvoluted S 2p (Fig. 1(c)) binding energy peaks of the sulfonic acid (–SO$_3$H) group were observed at 167.4 and 168.4 eV for $2p_{3/2}$ and $2p_{1/2}$, respectively, which are slightly lower than the reported values [11]. The deconvoluted O 1 s peaks (Fig. 1(d)) at 531.3 eV and 532.5 eV were assigned to C–OH and S—O bonds, respectively [11]. The lowered binding energy could be attributed to an increase in electronic density [54,55], indicative of a charge transfer from the phenyl ring in the S-CPOP framework to the sulfonic acid.

Fig. 2(a) shows the FT-IR spectra of S-CPOP in comparison with its precursor chemicals such as binaphthol and sulfonic acid: (i) a peak at 2925 cm^{-1} could be originated from C—H vibration peak in the methylene group [39], (ii) peaks at 1116 and 1033 cm^{-1} corresponded to the stretching vibrations of the S=O bond in the SO$_3$H group [11], (iii) bands at 1501 and 1316 cm^{-1} could be originated from the N=N and C—N stretches, respectively [56], and (iv) peaks at 3427 and 3276 cm^{-1} could be originated from the stretching vibration of two phenolic

hydroxyl groups [57]. Elemental analysis of S-CPOP revealed a composition of C (68.21 %), H (5.95 %), N (2.82 %), and S (3.16 %), deriving that 0.99 mmol g^{-1} of SO$_3$H moieties was functionalized in the CPOP. The amount of Brønsted and Lewis acids in the S-CPOP catalyst was estimated using the FT-IR spectrum of the pyridine-adsorbed S-CPOP catalyst (Fig. S1(a)). The characteristic broad vibration band at 1548 cm^{-1} and the sharp peak at 1439 cm^{-1} are attributed to pyridine adsorbed on the Brønsted and Lewis acid sites of the CPOP, respectively, due to the formation of pyridinium ions [58]. Based on the areas of these peaks, the amounts of Brønsted and Lewis acids in the S-CPOP catalyst were estimated to be 1.33 mmol g^{-1} and 1.24 mmol g^{-1}. The XRD pattern of S-CPOP (Fig. 2(b)) displayed three broad peaks at around 11°, 21°, and 44°, revealing that the material framework exhibits direct phenyl ring-ring interactions, intrinsic flexibility, and a disordered linkage structure, characteristic of an amorphous nature [59]. The porous properties were determined by N$_2$ sorption isotherm (Fig. 2(c)), which are summarized in Table 1. The S-CPOP catalyst exhibited a type-IV isotherm with an H3 hysteresis loop, implying the presence of both micropore and mesopore. Because of such a hierarchically nanoporous structure, the S-CPOP possessed a high BET surface area of 1050 m^2 g^{-1} and a large mesopore volume of 0.84 cm^3 g^{-1}. The pore size distribution plot revealed a prominent peak at 0.71 nm, along with several smaller
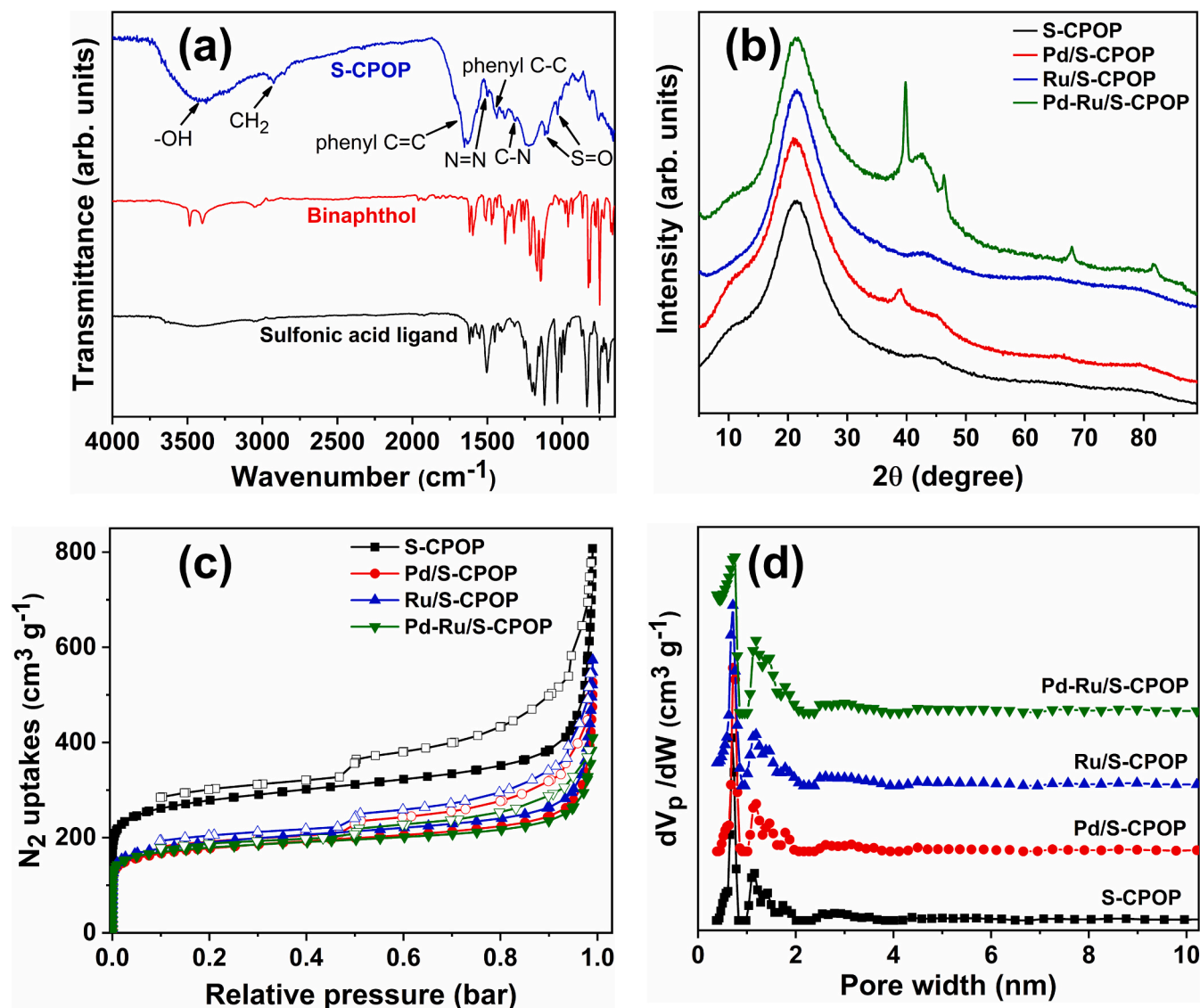

Fig. 2. (a) FT-IR spectra, (b) powder XRD patterns, (c) N$_2$ sorption isotherms, and (d) pore size distribution plots of S-CPOP and metal-loaded S-CPOP catalysts.

Table 1

Porous properties of the synthesized catalysts.

| Catalysts	S_{BET}[a] $(m^2\,g^{-1})$	V_{tot}[b] $(cm^3\,g^{-1})$	V_{micro}[c] $(cm^3\,g^{-1})$	V_{meso}[d] $(cm^3\,g^{-1})$	V_{meso}/V_{tot}
S-CPOP	1050	1.25	0.41	0.84	0.67
Pd/S-CPOP	661	0.87	0.27	0.60	0.69
Ru/S-CPOP	698	0.78	0.26	0.52	0.67
Pd-Ru/S-CPOP	672	0.66	0.26	0.40	0.61

[a] S_{BET} = BET surface area.

[b] V_{tot} = total pore volume calculated at a relative pressure of 0.99 bar.

[c] V_{micro} = micropore volume calculated at a relative pressure of 0.10 bar.

[d] V_{meso} (mesopore volume) = $V_{tot} - V_{micro}$.

peaks in both the micropore and mesopore regions (Fig. 2(d)). The FESEM images of S-CPOP displayed aggregated spherical particles with flower-like surface textures (Fig. 3(a)). EDS mapping showed that N, O, and S, along with C atoms, were uniformly distributed throughout the polymer network, confirming the presence of SO₃H groups on the surface of the S-CPOP material (Fig. 3(b–f)).

As characterized above, the S-CPOP consisted of sulfonic acid moieties with various organic functional groups on a wide surface of the organic framework, which could be potentially used for the design of multifunctional catalysts. More specifically, the abundant hydroxyl and azo groups could be used to support metal nanoparticles via the post-metallation process (step II in Scheme 1). After metallation, the FT-IR spectra of the Pd/S-CPOP, Ru/S-CPOP, and Pd-Ru/S-CPOP catalysts (Fig. S2(a)) revealed slight shifts in the characteristic peaks corresponding to the phenolic hydroxyl group, the N=N bond, and the C—N bond stretching vibrations, compared to the pristine S-CPOP material without metallation. These shifts suggest that the metallic Pd and Ru particles are strongly bound to the surface functional groups of the S-CPOP. The amounts of Brønsted and Lewis acids in the Pd-Ru/S-CPOP catalyst were estimated to be 1.02 mmol g⁻¹ and 3.31 mmol g⁻¹, respectively, from FT-IR spectrum of the pyridine-adsorbed Pd-Ru/S-CPOP catalyst (Fig. S1(b)). The elemental states, compositions, the nature of chemical bonds, and surface exposed metallic amounts in Pd/S-CPOP, Ru/S-CPOP, and Pd-Ru/S-CPOP catalysts were analyzed using XPS (Figs. S3 and Fig. 4), and the results are listed in Tables S1 and S2. The Pd/S-CPOP catalyst exhibited two prominent peaks at binding energies of 334.78 and 340.28 eV for the $3d_{5/2}$ and $3d_{3/2}$ states of Pd(0) (Fig. 4(a)) [60]. Additionally, weak doublet peaks were observed at 336.58 and 342.18 eV, attributed to the $3d_{5/2}$ and $3d_{3/2}$ states of Pd(II) ions. This suggests the presence of a small amount of unreduced Pd(II) bound to the support material. Similarly, Fig. 4(b) displays two binding energy peaks at 461.98 and 484.28 eV, attributed to the $3p_{3/2}$ and $3p_{1/2}$ states of Ru(0) in Ru/S-CPOP. Minor peaks at 465.28 and 487.78 eV were also observed, which are attributed to Ru(IV) ions, likely due to

surface oxidation under exposure to moisture [61,62]. The deconvoluted XPS of the C 1s - Ru 3d, N 1s, and S 2p regions for the Pd-Ru/S-CPOP catalyst (Fig. S3(a–c)) did not show significant peak shifts compared to those of the pristine S-CPOP support (Fig. 1(a–c)). However, the deconvoluted peaks at 530.78 and 532.18 eV in the O 1s XPS of Pd-Ru/S-CPOP catalyst in Fig. S3(d) were slightly downshifted compared to those in the pristine S-CPOP support in Fig. 1(d), indicating a change in electronic interactions probably due to the metal binding. Notably, the $3d_{3/2}$ peak overlaps with the C 1s peaks. The XPS analysis of the bimetallic Pd–Ru/S-CPOP catalyst reveals distinct binding energy shifts compared to the corresponding monometallic Pd/S-CPOP and Ru/S-CPOP catalysts (Fig. 4), with the corresponding binding energy values listed in Table S2. The Pd 3d peaks shift to higher binding energies at 335.38/340.58 eV for Pd(0) and 337.08/342.78 eV for Pd(II) ions (Fig. 4(a)), indicating a decrease in electron density on the Pd surface. In contrast, the Ru 3p peaks shift to lower binding energies at 461.58/483.88 eV for Ru(0) and 464.78/486.98 eV for Ru(IV) ions (Fig. 4(b)), suggesting an increase in electron density on the Ru atoms. These reciprocal shifts strongly support the effective electron transfer from Pd to Ru atoms, consistent with previous reports [63,64]. As a result of this charge redistribution, the Pd becomes more electron-deficient, lowering its d-band center and consequently weakening its interaction with electron-accepting O₂ species. Conversely, the increased electron density on Ru raises its d-band center, which enhances its ability to donate electrons to the antibonding orbitals of O₂ and thus facilitates O₂ activation [63]. Furthermore, the electron-deficient Pd surface can interact favorably with the electron-rich hydroxyl group of the HMF substrate, as discussed in the mechanistic section. This electronic synergy between Pd and Ru plays a crucial role in the enhanced catalytic performance observed in aerobic oxidation reactions. These FT-IR and XPS results also confirm that the Pd and Ru particles are strongly bound on the hydroxyl group of the support material without inducing significant structural changes in the catalyst.

The XRD pattern of the mono-metallic Pd/S-CPOP and Ru/S-CPOP displayed peaks at 39.0° and 42.9° corresponding to the face-centered cubic (fcc) structure of Pd(111) and the hexagonal close-packed (hcp) structure of Ru(002) planes, respectively (Fig. 2(b)) [65,66]. In contrast, the bimetallic Pd-Ru/S-CPOP exhibited strong diffraction peaks at 39.9°, 46.3°, 67.9°, and 81.7°, which are attributed to the fcc of Pd(111), Pd (200), Pd(220), and Pd(311), respectively (Fig. 2(b)) [65]. A weak peak at 42.5° was observed, corresponding to the hcp of Ru(002) lattice. The positions of these peaks were slightly shifted relative to those of the monometallic Ru and Pd NPs [67]. As shown in Fig. 2(c), the BET surface areas decreased to 661, 698, and 672 m² g⁻¹ for the Pd/S-CPOP, Ru/S-CPOP, and Pd-Ru/S-CPOP catalysts, respectively, compared to the pristine support. This reduction is attributed to the increased sample mass and partial pore-filling by the Pd and Ru NPs. The pore size distribution plots showed no significant changes, indicating that the Pd and Ru NPs are primarily located on the surface of the support material (Fig. 2(d)). This observation is consistent with the fact that the particle sizes of Pd and Ru NPs are relatively larger than the pore size of the support, as confirmed by FETEM images (Fig. 5(a–l)). Particle size distribution histogram of Pd/S-CPOP, Ru/S-CPOP, and Pd-Ru/S-CPOP was performed using low-magnification FETEM images, as shown in Fig. 5 (m–o). The Ru/S-CPOP and Pd-Ru/S-CPOP catalysts exhibited a mean particle size of around 4 nm with homogeneous dispersion, while the Pd/S-CPOP showed an average size of approximately 7 nm. This result indicates that the Pd particle size decreased from ~7 nm to ~4 nm upon incorporation of Ru NPs, indicating that Ru effectively enhances the dispersion of Pd on the S-CPOP support network. This behavior is consistent with the previous report [35]. The FESEM images and STEM with EDS mapping images of Pd-Ru/S-CPOP further confirm the homogeneous dispersions of Pd and Ru atoms on the surface of the S-CPOP polymer network (Figs. S4 and Fig. 6). The metal loadings on S-CPOP support were estimated by ICP–OES to be 1.92 wt% for Pd, 1.87 wt% for Ru, and 0.90/0.98 wt% for Pd/Ru in the Pd/S-CPOP, Ru/S-CPOP, and
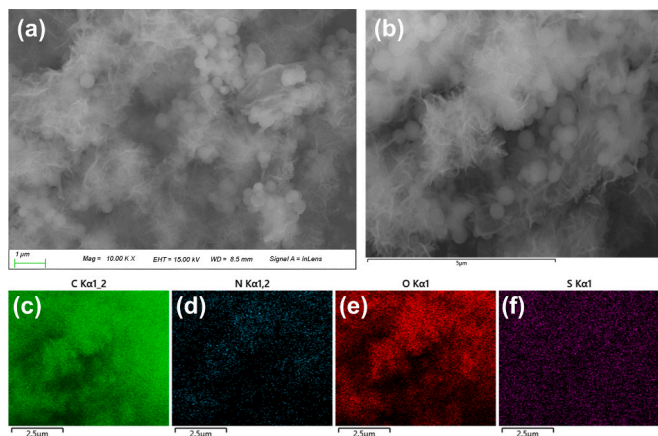
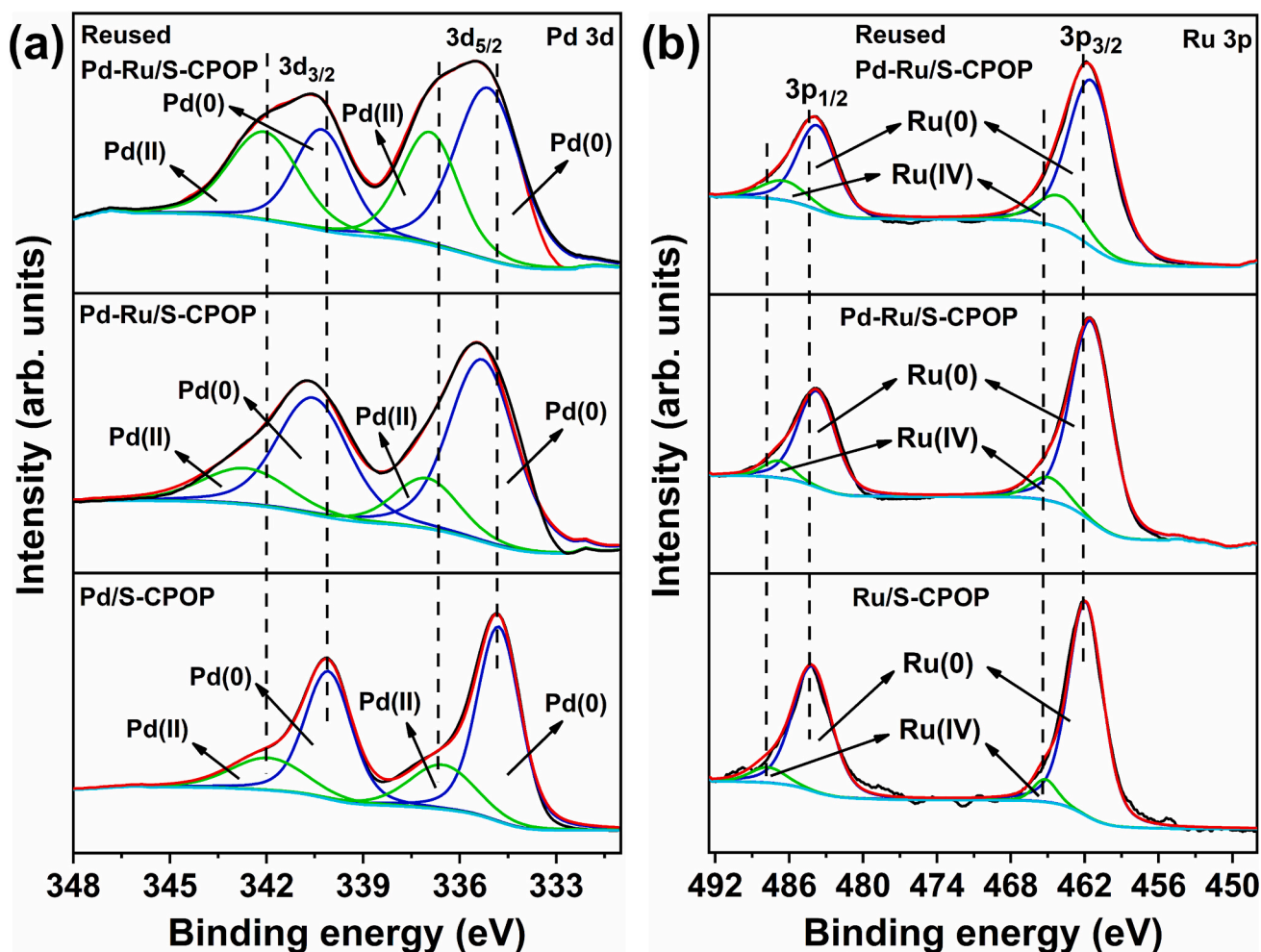**Fig. 3.** (a) FESEM and (b–f) EDS mapping images of S-CPOP.

Fig. 4. Deconvoluted XPS of (a) Pd 3d and (b) Ru 3p core level of Pd/S-CPOP, Ru/S-CPOP, and Pd-Ru/S-CPOP catalysts.

Pd-Ru/S-CPOP, respectively. The mass ratio of the Pd, Ru, and Pd-Ru in S-CPOP for Pd/S-CPOP, Ru/S-CPOP, and Pd-Ru/S-CPOP was 1.96:100, 1.91:100, 0.91:0.99:100, respectively.

3.2. Reaction studies

The successive conversion of fructose to FDCA via HMF involves two distinct catalytic processes (Scheme 2), each requiring unique catalytic sites [15,34]. In the first step, fructose undergoes dehydration to form HMF, catalyzed by acid sites. In the second step, HMF is converted to FDCA via an aerobic oxidation process, catalyzed by metal NPs with oxidation ability in the presence of O_2. To achieve the successful direct conversion of fructose to FDCA via HMF, not only the individual catalytic sites but also many requirements should fit satisfactorily. Two different catalytic sites for two distinct reaction steps should exist, with balanced catalytic interplays between them. Each reaction process always produces undesired byproducts, in which the reaction pathways for the byproduct formation should be carefully controlled for achieving a high yield of the desired product, i.e., FDCA. To make it feasible, the reaction thermodynamics and kinetics should be delicately controlled by adjusting the reaction conditions and catalysts. Based on this rationale, we approached the catalyst design by systematic investigations of individual reaction processes, i.e., fructose dehydration and HMF oxidation.

3.2.1. Dehydration of fructose

One of the crucial issues in HMF production is the acidity of the catalyst used for fructose conversion to HMF (Scheme 3). Organic acids are easier to handle and less corrosive than strong mineral acids [68,69]. With this in mind, we investigated S-CPOP as the organic-acid functionalized heterogeneous catalyst for the dehydration of fructose (2 mmol) to HMF under various conditions, as summarized in Table 2. Without the addition of a catalyst, the reaction yielded only 7 % HMF in DMSO solvent at 130 °C for 1 h (entry 1 in Table 2). In contrast, with the S-CPOP catalyst (60 mg), 90 % conversion of fructose was achieved, yielding 83 % HMF along with byproducts such as LA (2 %), FA (2 %), and others (entry 2 in Table 2). Other byproducts may include humins, although their quantities could not be determined [11,70]. The LA and humins are typically formed via the rehydration of HMF, involving nucleophilic attack or aldol condensation, which can subsequently polymerize into oligomers [50]. The susceptibility of HMF to nucleophilic attack is fundamentally governed by its lowest unoccupied molecular orbital (LUMO) energy, as molecules with lower LUMO energy are more electrophilic nature and thus more reactive. The highly polar aprotic DMSO solvent plays a crucial role in stabilizing HMF via H-bonding interactions with its carbonyl and hydroxyl groups. This interaction not only enhances HMF solubility but also increases its LUMO energy level, thereby reducing its electrophilicity and susceptibility to nucleophilic attack [51,71]. As a result, the formation of humins was suppressed during the reaction. When other polar solvents, including water, DMF, acetonitrile (CH_3CN), and tetrahydrofuran (THF), were used (entries 3–6 in Table 2), fructose conversion decreased compared to the use of DMSO. This is likely due to the bi-heteroatom (O and S) of DMSO, which can destabilize protons of the sulfonic acid group
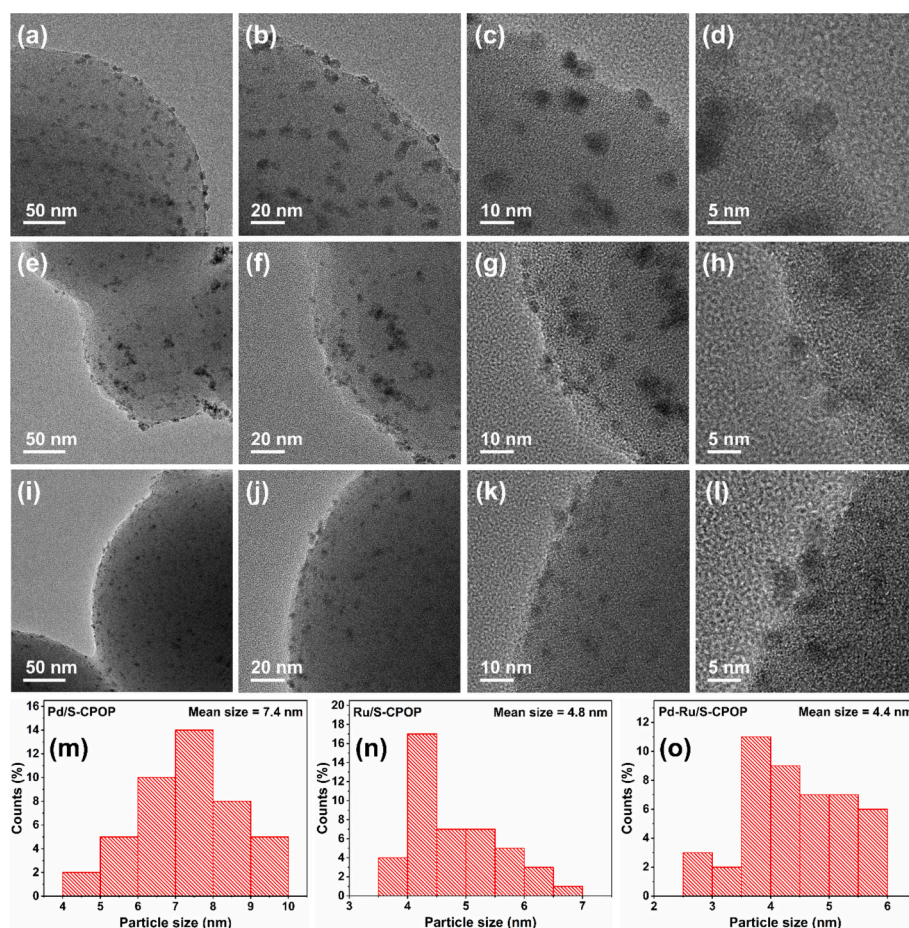
Fig. 5. FETEM images of (a–d) Pd/S-CPOP, (e–h) Ru/S-CPOP, and (i–l) Pd-Ru/S-CPOP, along with particle size distribution histograms of (m) Pd/S-CPOP, (n) Ru/S-CPOP, and (o) Pd-Ru/S-CPOP catalysts.
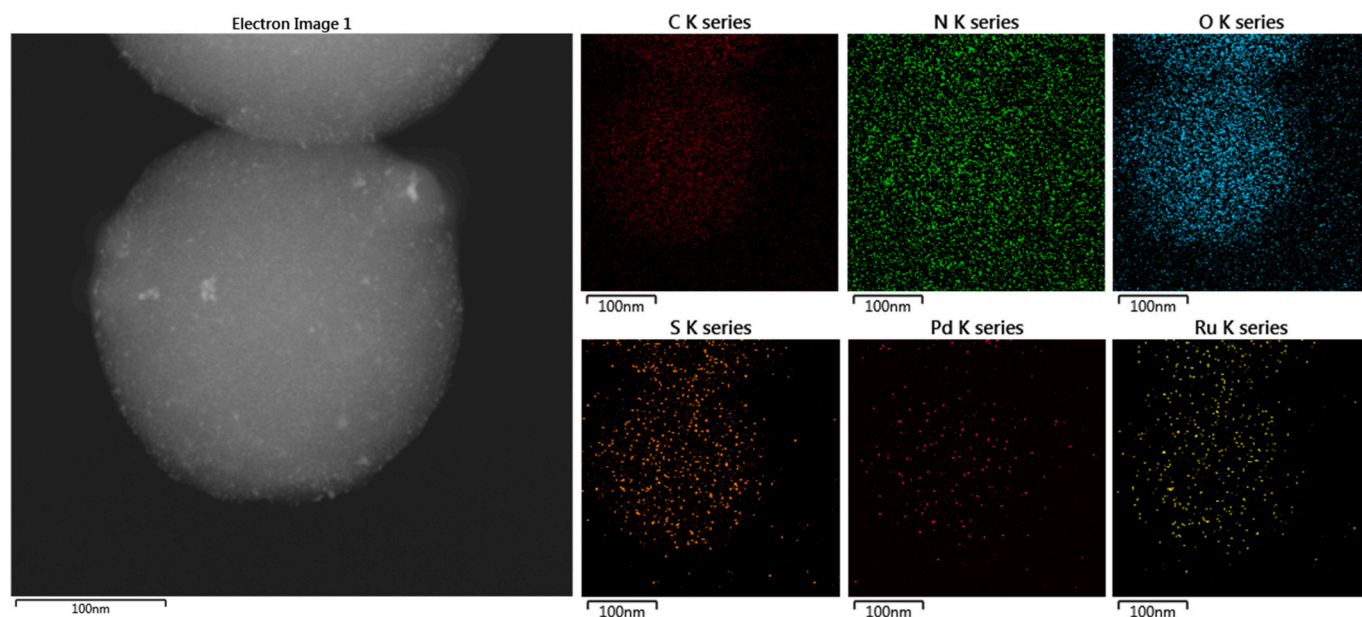

Fig. 6. STEM-EDS mapping images of the Pd-Ru/S-CPOP catalyst.

in the S-CPOP catalyst, facilitating their interaction with fructose and promoting its conversion to HMF [72,73]. Note that the HMF selectivity was also high when water was used as the solvent (entry 3 in Table 2), but the high polarity of water lowered the catalytic activity of sulfonic acid in S-CPOP and hence the HMF yield was close to half of that achieved when DMSO was used as solvent (entry 2 vs. 3 in Table 2).
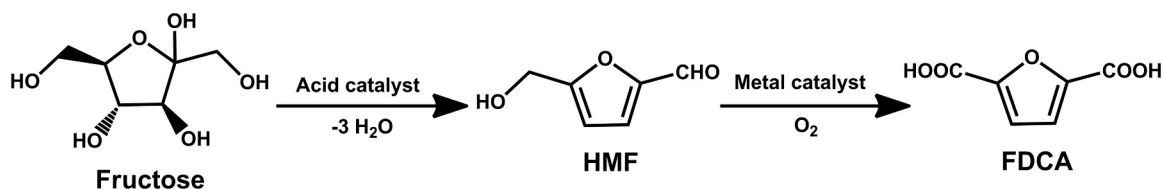
Scheme 2. Direct synthesis of FDCA from fructose via HMF as the intermediate species.
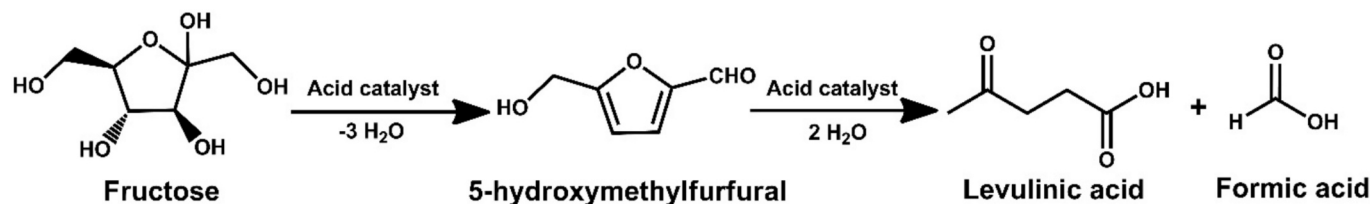
Scheme 3. Dehydration of fructose to HMF and other byproducts (levulinic acid and formic acid) that could be produced via an undesired rehydration reaction.

Table 2
The catalytic activity of S-CPOP for the dehydration of fructose to HMF.[a]

Entry	Catalyst	Solvent (mL)	Conversion[b] (%)	Products yield[b] (%)		HMF Selectivity[c] (%)	CB[d] (%)
				HMF	LA + FA		
1	–	DMSO	8	7	–	88	99
2	S-CPOP	DMSO	90	83	4	92	97
3	S-CPOP	Water	56	44	6	79	94
4	S-CPOP	DMF	69	56	8	81	95
5	S-CPOP	CH3CN	21	13	4	62	96
6	S-CPOP	THF	15	10	2	67	97
7	S-CPOP	D:W[e] (4:1)	99	88	6	89	95
8	S-CPOP	D:W (3:2)	98	92	4	94	98
9	S-CPOP	D:W (2:3)	85	75	6	88	96
10	S-CPOP	D:W (1:4)	74	63	4	85	93
11	Pd/S-CPOP	D:W (3:2)	99	90	2	91	93
12	Ru/S-CPOP	D:W (3:2)	100	88	–	88	88
13	Pd-Ru/S-CPOP	D:W (3:2)	100	87	2	87	89

[a] Conditions: Catalyst (60 mg), fructose (2 mmol), molar ratio of fructose/acid content in catalyst (34:1), solvent (5 mL), temp. (130 °C), and time (1 h).
[b] Conversion of fructose and yield of products were calculated by the quantitative method from the calibration curve of the standard solution of respective compounds.
[c] Selectivity of HMF was calculated using Eq. (3).
[d] CB was calculated using Eq. (5).
[e] D:W, DMSO:water (v/v).

To achieve high fructose conversion while maximizing HMF yield, it is essential to optimize the fructose dehydration and minimize the HMF rehydration into byproducts. Tuning the solvent polarity of the reaction medium, the different volume ratios of DMSO and water were used to construct the optimized reaction environment. When a DMSO:water (4:1, v/v) solvent mixture was used, the HMF yield increased to 88 % (entry 7 in Table 2). Increasing water content to a 3:2 (DMSO:water; v/v) ratio further improved the HMF yield to 92 % (entry 8 in Table 2) along with the formation of small amounts of byproducts such as LA, FA, and others. The improvement in fructose conversion and HMF yield can be attributed to the enhanced solubility and mobility of fructose into the active sites of the catalyst. After recovering the catalyst by centrifugation, FT-IR analysis was performed to assess its structural stability and to check for the presence of insoluble humins (Fig. S2(b)). No structural changes or humin-related stretching vibration peaks were observed, indicating that the catalyst remained highly stable and that no insoluble humins were present in the catalyst. In addition, pyridine-adsorbed S-CPOP analyzed after the catalytic process exhibited a nearly identical distribution of Brønsted acid (1.33 mmol g^{-1}) and Lewis acid (1.23 mmol g^{-1}) sites compared to the fresh one, indicating no significant loss of sulfonic acid moieties during the catalytic process (Fig. S1(a)). Further increases in water content led to decreased fructose conversion

and HMF selectivity (entries 9–10 in Table 2), due to the formation of side products such as LA, FA, and humins [20]. These findings suggest that the amount of water is crucial for maximizing fructose dehydration and minimizing the byproduct formation via rehydration of the desired HMF. Additionally, fructose conversion was tested using Pd/S-CPOP, Ru/S-CPOP, and Pd-Ru/S-CPOP catalysts, which gave 90, 88, and 87 % HMF yield, and 5, 9, and 10 % DFF yield, respectively (entries 11–13 in Table 2). The noticeable formation of DFF is likely due to the oxidation of HMF, which can be attributed to the oxidation catalytic ability of metal NPs in S-CPOP catalysts [74,75].

The effect of stirring on the conversion of fructose (2 mmol) was investigated using the S-CPOP catalyst (60 mg) in DMSO:water (v/v; 3:2) solvent mixture at 130 °C for 1 h, to evaluate the influence of mass transfer resistance on the reaction rate. As shown in Fig. S5, no significant change in fructose conversion was observed across varying stirring speeds, indicating that the reaction proceeds under a kinetically controlled regime, with the rate governed predominantly by the intrinsic catalytic activity rather than by external mass transfer limitations. Therefore, all subsequent catalytic experiments were performed at a fixed stirring speed of 400 rpm to ensure consistency in kinetic evaluation. The effect of the catalyst amount on fructose conversion and HMF yield is displayed in Fig. 7(a). As the catalyst loading increased
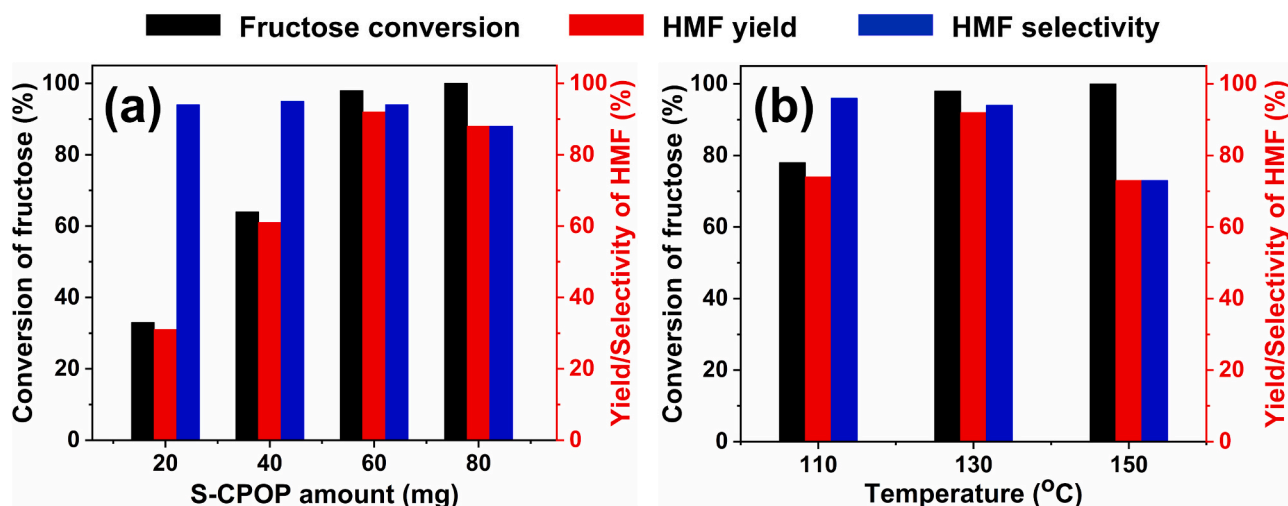
Fig. 7. (a) Effect of S-CPOP catalyst loading and (b) effect of temperature on the dehydration of fructose to HMF.

from 20 to 40 and 60 mg, the fructose conversion also increased proportionally from 33 % to 64 % and 98 %, respectively, with corresponding HMF yields of 31 %, 61 %, and 92 % after 1 h. This improvement is attributed to the enhanced accessibility of active sites in the catalyst. Nevertheless, a decreased HMF yield was observed for further increases in catalyst loading, revealing that the excess catalyst accelerated the rehydration of HMF, leading to the formation of byproducts like LA and FA (Scheme 3). The fructose dehydration reaction was then examined for 1 h at three different temperatures of 110, 130, and 150 °C, with optimized catalyst loading (60 mg) and DMSO: water (v/v; 3:2) solvent mixture. Fig. 7(b) showed that the fructose conversion and HMF yield increased as the temperature was raised from 110 to 130 °C, and then HMF yield decreased at 150 °C, indicating that the excess heating would promote side reactions such as the formation of LA, FA, and humins via the hydration of HMF and thereby decrease HMF yield. The effect of reaction time on fructose conversion and HMF yield was also studied under the optimal catalyst amount and solvent at 130 °C. Fig. 8 illustrates the time-dependent conversion of fructose and the yield of HMF. Both fructose conversion and HMF yield increased linearly with time up to 50 min, reaching a maximum conversion of 98 % and an HMF yield of 96 %. After 50 min, the HMF yield began to decline slightly, despite complete conversion of fructose. Fructose conversion was also monitored using nuclear magnetic resonance (NMR) spectroscopy (Fig. S6). These results demonstrate that the excessive

catalyst loading, high reaction temperature, and longer reaction time facilitated the rehydration of HMF to byproducts like LA, FA, and humins, and also proved the sensitivity of the dehydration process to achieve a high HMF yield. Finally, we obtained a maximum fructose conversion of 98 % with an HMF yield of 96 % under the optimized reaction conditions, including S-CPOP amount (60 mg), DMSO:water (v/v; 3:2), temperature (130 °C), and reaction time (50 min).

To gain insights into the reaction competitiveness and energy values for fructose conversion, the kinetics studies were executed at different loadings of S-CPOP catalyst and within a temperature range of 110–150 °C, assuming that all side reactions and byproducts were negligible. Before these calculations, the reaction was performed with different fructose amounts (Fig. S7(a)) under the optimized catalyst amount (60 mg) and temperature (130 °C). The rate constants were calculated using Eqs. (10) and (11) [39], and the derived constants are listed in Table 3. Fig. S7(b–c) showed a linear fit of fructose conversion versus reaction time, confirming that the reaction follows first-order kinetics with respect to fructose concentration.

$$rate = k[\text{fructose}]^a[\text{S} - \text{CPOP}]^b \qquad (10)$$

$$rate = k_{obs}[\text{fructose}]^a \qquad (11)$$

where $k_{obs} = k[\text{S} - \text{CPOP}]^b$
So,

$$\ln(k_{obs}) = \ln(k) + b\ln[\text{S} - \text{CPOP}] \qquad (12)$$

$$\ln(k_{obs}) = -\left(\frac{E_a}{RT}\right) + \ln(A) \qquad (13)$$

where k_{obs}, R, T, A, and E_a are the rate constant (s^{-1}), gas constant (0.008314 kJ mol^{-1} K^{-1}), temperature (K), Arrhenius constant (s^{-1}), and activation energy (kJ mol^{-1}), respectively.

Fig. 8. Time course of fructose dehydration to HMF over S-CPOP catalyst at 130 °C.

Table 3
Rate constants for the dehydration of fructose and the oxidation process of HMF to FDCA.

No.	Temp. (K)	Rate constant (s^{-1})	Rate constant (h^{-1})		
		Fructose to HMF (k_{obs})	HMF to DFF (k_1)	DFF to FFCA (k_2)	FFCA to FDCA (k_3)
1	383	2.8736	0.6084	0.1889	0.0480
2	403	5.4366	1.1712	0.6532	0.3230
3	423	6.6542	1.9661	1.3438	0.9863

$$\ln\left(\frac{k_{obs}}{T}\right) = \ln\left(\frac{k_B}{h}\right) + \frac{\Delta H^*}{R} - \frac{\Delta H^*}{RT} \tag{14}$$

where h, k_B, ΔH^*, and ΔS^* are the Planck's constant (6.626×10^{-34} J s), and Boltzmann constant (1.381×10^{-23} J K^{-1}), activation enthalpy (kJ mol^{-1}), activation entropy (J mol^{-1} K^{-1}), respectively.

$$\text{Gibbs free energy } (\Delta G^*) = -RT\ln\left(\frac{hk_{obs}}{Tk_B}\right) \tag{15}$$

The kinetics of fructose conversion were also investigated with different S-CPOP loading experiments with the fructose amount of 2 mmol at 130 °C, showing a linear increase of fructose conversion as a function of reaction time and catalyst amount (Fig. S8(a)). Fig. S8(b–c) showed the first-order kinetics for the S-CPOP catalyst using Eq. (12), revealing that a sulfonic acid moiety is involved mainly in the fructose dehydration process. Further, the thermodynamic parameters for the fructose conversion to HMF were calculated using the Arrhenius Eq. (13), the linearized form of the Eyring Eq. (14), and the Gibbs free energy Eq. (15) to determine the feasibility of the reaction [76,77], from which the derived values are listed in Table 4. Temperature-dependent kinetic experiments (Fig. S9(a–b)) were studied to derive the E_a for the fructose dehydration process. A linear fitting as functions of $\ln(k_{obs})$ vs $-1/RT$ derived the E_a of 28.49 kJ mol^{-1} (Fig. S9(c)), suggesting that the fructose dehydration reaction is more feasible within this temperature region.

The ΔH^* and ΔS^* values were found from the linear correlation plots (Fig. S9(d)) of $\ln(k_{obs}/T)$ vs $-1/RT$, in which the slope of the plot corresponds to ΔH^*, and the intercept $\left(\ln\left(\frac{k_B}{h}\right) + \frac{\Delta S^*}{R}\right)$ was used to estimate the ΔS^* value. The resultant positive value of ΔH^* (25.15 kJ mol^{-1}) for fructose conversion was very close to the activation energy, revealing that the reaction is endothermic and requires external energy to form the catalyst–fructose complex transition state [78]. On the other hand, the calculated ΔS^* value of -248.60 J mol^{-1} K^{-1} indicates that the reaction system is more ordered in the transition state than in the ground state and has a non-spontaneous nature (see page S11 in Supporting Information for calculation details) [79]. The ΔG^* value for the fructose conversion at 130 °C was calculated to be 124.90 kJ mol^{-1} using Eq. (15), which also confirms the non-spontaneous nature of the reaction (see page S11 in Supporting Information for calculation details). The catalytic performance of the S-CPOP catalyst in the dehydration of fructose to HMF was compared with previously reported solid catalysts (Table S3). Many of these studies did not report the amount of acid sites in their catalysts, limiting the ability to calculate the TOF values and directly compare catalyst efficiencies. In contrast, the S-CPOP catalytic system achieved a high HMF yield (96 %) and a high TOF (38.0 h^{-1}) at 130 °C, along with easy catalyst preparation and separation compared to other systems.

3.2.2. Aerobic oxidation of HMF

During the oxidation of HMF to FDCA, sequential oxidation processes are followed as schematized in Scheme 4; (i) oxidation of hydroxyl group in HMF to an aldehyde group, forming DFF, (ii) oxidation of one aldehyde group in DFF to the carboxylic acid group, forming

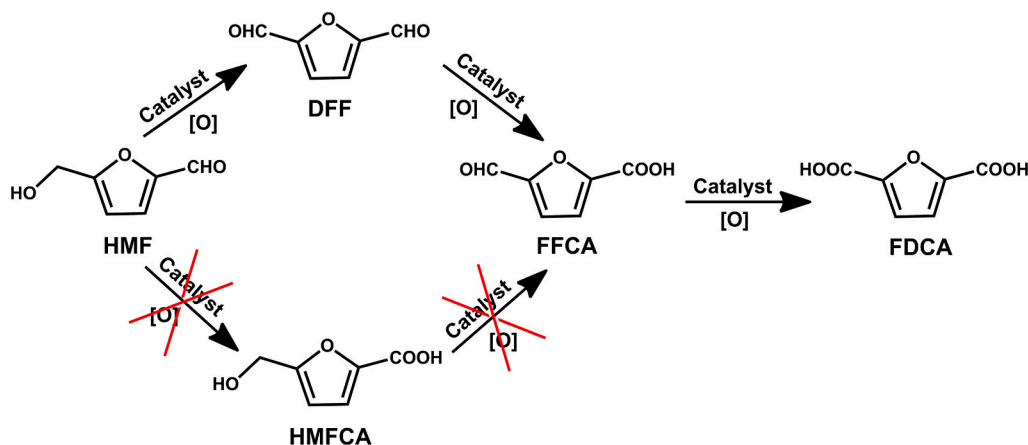FFCA, and (iii) oxidation of the remaining aldehyde group in FFCA to the carboxylic acid group, forming FDCA. In such stepwise oxidation reaction processes, electron-deficient metal ions and/or NPs are highly desirable. To evaluate the catalytic efficiency of the prepared S-CPOP-supported Pd and Ru NPs catalysts under base-free conditions, the oxidation of HMF (2 mmol) was conducted under O$_2$ (10 bar) in the DMSO:water (v/v; 3:2) solvent mixture. The monometallic Pd/S-CPOP (molar ratio of HMF to Pd is 185:1) and Ru/S-CPOP (molar ratio of HMF to Ru is 180:1) catalysts (60 mg) gave only 63 and 78 % of HMF conversion with FDCA/FFCA yields of 22/40 % and 43/35 %, respectively, after 6 h at 130 °C (Fig. 9(a)). These results suggest that the monometallic Pd and Ru were ineffective in further oxidizing FFCA to FDCA. This limitation may be due to a possible interaction between the metals and the carboxylic acid group in FFCA, which could inhibit the interaction of the FFCA aldehyde group with the active metallic sites [35]. In contrast, the bimetallic Pd-Ru/S-CPOP (the molar ratio of HMF/(Pd + Ru) is 184:1) catalyst gave almost the full conversion of HMF with a 98 % yield of FDCA (Fig. 9(a)). No hydrated products were observed, likely due to the strong binding affinity of HMF to the Ru and Pd surfaces, which inhibits its interaction with sulfonic acid groups. The significant enhancement in FDCA yield could be attributed to the synergistic effect of electron transfer between Pd and Ru NPs, as well as their close proximity, which promotes the adsorption of the aldehyde group in FFCA to active metallic sites, thus facilitating oxidation to FDCA. In contrast, the physical mixture of monometallic Pd/S-CPOP (30 mg; molar ratio of HMF to Pd is 92:1) and Ru/S-CPOP (30 mg; molar ratio of HMF to Ru is 90:1) resulted in complete HMF conversion but yielded only 81 % FDCA under identical conditions (130 °C, 6 h; Fig. 9 (a)). This lower FDCA yield was ascribed to the spatial separation of Pd and Ru NPs in the physical mixture, which restricts the cooperative catalytic interactions that are present in the bimetallic system. To gain further insight into the influence of Pd and Ru composition on catalytic performance, the reaction was performed using two bimetallic Pd-Ru/S-CPOP catalysts with varying Pd-to-Ru molar ratios (0.5:1.5 and 1.5:0.5). These Pd$_{0.5}$-Ru$_{1.5}$/S-CPOP and Pd$_{1.5}$-Ru$_{0.5}$/S-CPOP catalysts gave 86 % and 74 % HMF conversion with 67 % and 51 % FDCA yields, respectively (Fig. 9(b)). Compared to the equimolar Pd-Ru system, these catalysts exhibited lower activity and selectivity, highlighting the critical role of balanced metal compositions. The results suggest that both Pd and Ru contribute cooperatively to the oxidation process, and an optimal 1:1 ratio is necessary to maximize the synergistic interactions that promote efficient transformation of HMF and its intermediates into FDCA. The effect of Pd-Ru/S-CPOP catalyst loading (Fig. 9(c)) on the oxidation of HMF to FDCA was next studied at 130 °C for 6 h. A lower catalyst loading of 20 mg resulted in only a 27 % yield of FDCA with a 67 % conversion of HMF. When the Pd-Ru/S-CPOP amount increased to 40 mg, the FDCA yield increased to 68 % with complete conversion of HMF. Further increase of the catalyst amount to 60 mg resulted in full HMF conversion, achieving a 98 % FDCA yield. These results suggest that higher catalyst loading provides more active Pd and Ru sites, thus promoting greater HMF conversion and higher FDCA yield. The influence of O$_2$ pressure on the oxidation of HMF was also examined using the optimized amount of Pd-Ru/S-CPOP catalyst at 130 °C for 6 h. As shown in Fig. 9(d), decreasing the O$_2$ pressure from 10 to 5 and 2 bar led to a substantial reduction in HMF conversion from 98 % to 78 % and 31 %, respectively. Correspondingly, the FDCA yield decreased to 52 % and 15 %. This reduction in both conversion and FDCA yield is attributed to the limited availability and adsorption of O$_2$ on the catalyst surface at lower pressures, which limits the overall oxidation efficiency.

The effect of reaction time was studied at three different temperatures using Pd-Ru/S-CPOP catalyst to observe the reaction intermediates in the oxidation of HMF to FDCA. At 110 °C (Fig. 10(a)), HMF conversion gradually increased, reaching a maximum at 4 h, while the formation of intermediates (DFF and FFCA) exhibited volcano-type curves with respect to reaction time. In contrast, the FDCA yield steadily increased as the intermediates decreased, reaching 61 % at 6 h. When

Table 4
Thermodynamic parameters for the dehydration of fructose and the oxidation process of HMF to FDCA.

Thermodynamic parameters	Reactions			
	Fructose to HMF	HMF to DFF	DFF to FFCA	FFCA to FDCA
E_a (kJ mol^{-1})	28.49	39.54	66.30	102.14
ΔH^* (kJ mol^{-1})	25.15	36.20	62.96	98.79
ΔS^* (J mol^{-1} K^{-1})	−248.60	−156.51	−95.91	−13.45
ΔG^* (kJ mol^{-1})	124.90	99.18	101.14	103.49

Scheme 4. Base-free aerobic oxidation of HMF to FDCA via DFF and FFCA as the intermediate species formed during sequential oxidation processes.
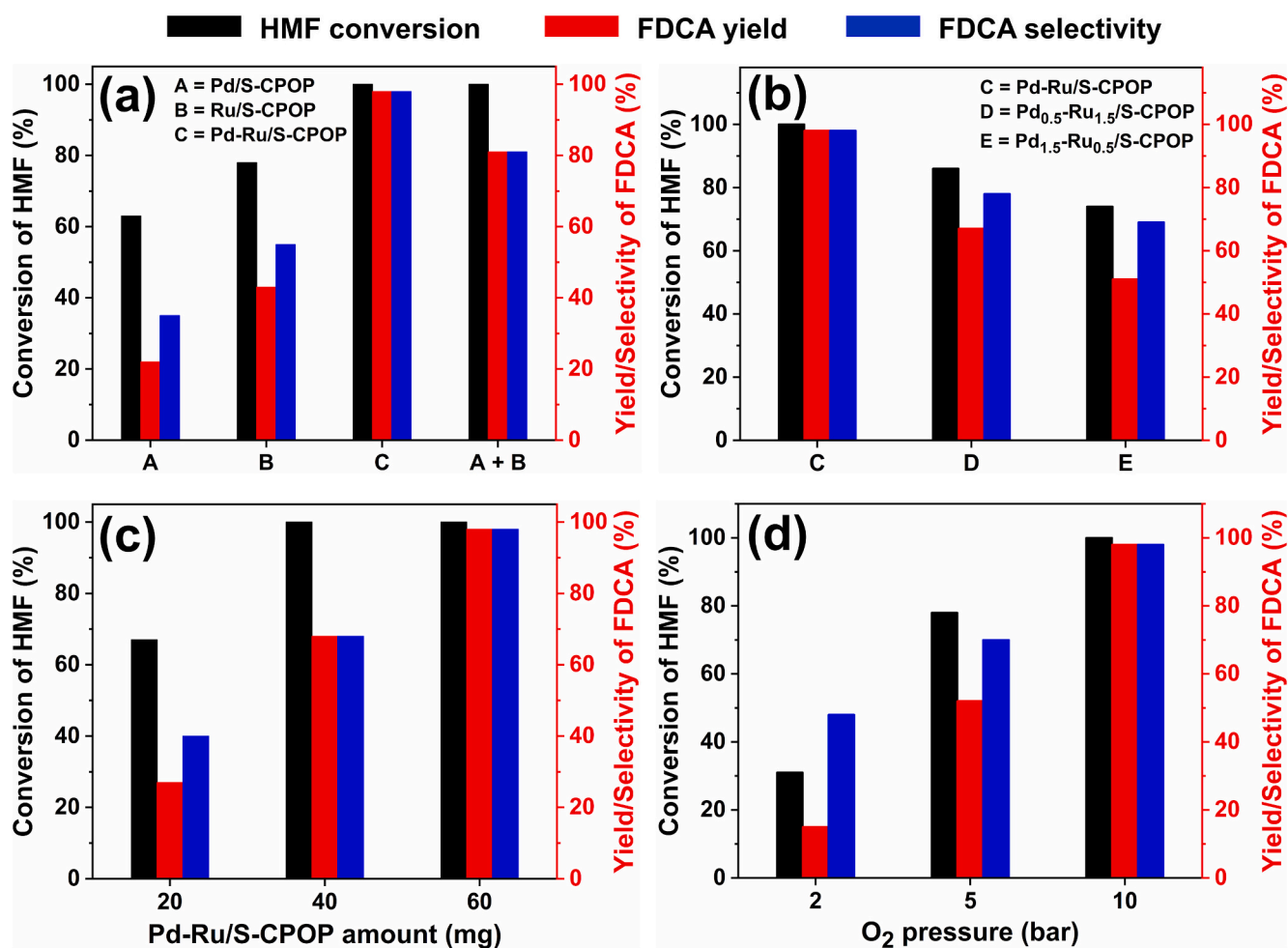

Fig. 9. (a) Effect of (a) different catalysts, (b) different molar ratio of Pd-to-Ru, (c) Pd-Ru/S-CPOP catalyst loading, and (d) O_2 pressure on the aerobic oxidation of HMF to FDCA.

the temperature was raised to 130 °C (Fig. 10(b)), HMF was fully converted within 2 h, accompanied by a rapid formation of intermediates. After this point, the yield of intermediates gradually decreased as FDCA formation accelerated, reaching a maximum at 6 h. These results indicate that the Pd-Ru/S-CPOP catalyst initially oxidized the terminal hydroxyl group of HMF to an aldehyde group (i.e., DFF) at a fast rate (within 2 h), followed by a slower oxidation to the carboxylic acid (i.e., FDCA) at a slow rate (over 6 h). These kinetic results proved that the

oxidation of HMF to FDCA over the Pd-Ru/S-CPOP catalyst occurred via the DFF and FFCA as intermediate species rather than through the formation of 5-hydroxymethyl-2-furancarboxylic acid (HMFCA) (Scheme 4). The reaction pathway was also monitored using NMR spectroscopy, confirming the presence of DFF and FFCA as the intermediate species and FDCA as the final product (Fig. S10). Further increase in temperature to 150 °C (Fig. 10(c)) resulted in a slight decrease in FDCA yield to 88 %, likely due to the formation of byproducts such as LA, FA, and
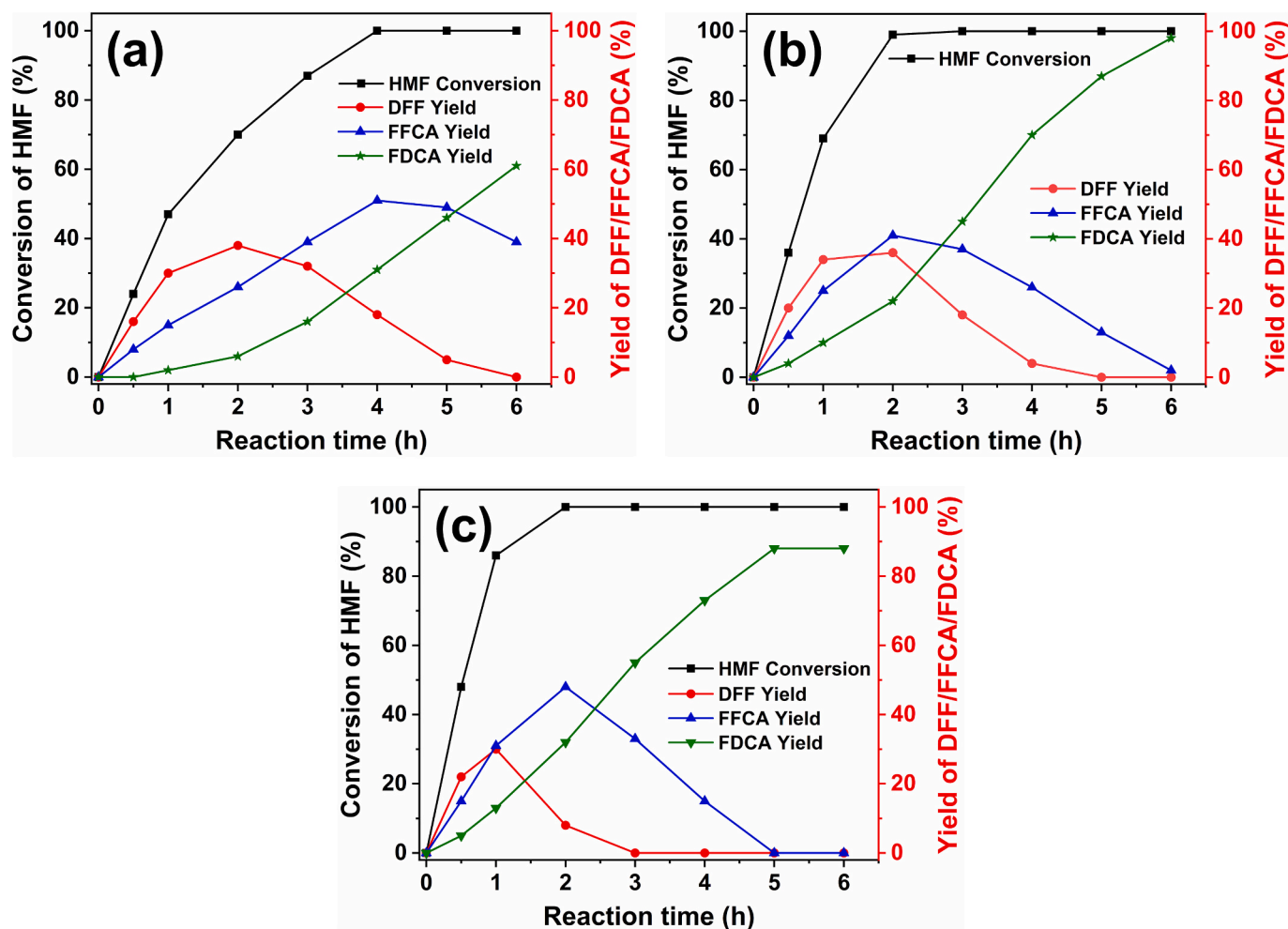
Fig. 10. Time courses for the oxidation of HMF to FDCA over Pd-Ru/S-CPOP catalyst at different reaction temperatures (a) 110 °C, (b) 130 °C, and (c) 150 °C.

humins (CB is 88 % under this reaction condition). This decline could be attributed to the rehydration of HMF catalyzed by the acidic groups on the Pd-Ru/S-CPOP catalyst. Thus, the optimized conditions for the aerobic oxidation of HMF to FDCA were established as follows: Pd-Ru/S-CPOP catalyst (60 mg), HMF (2 mmol), DMSO:water (v/v; 3:2), temperature (130 °C), and time (6 h). To further elucidate the reaction mechanism, the reactions were performed using the key intermediates DFF and FFCA as individual substrates under the optimized aerobic oxidation conditions. Both intermediates were efficiently converted to FDCA, with high yields of 98 % and 99 %, respectively. These results provide strong support for the proposed reaction pathway, confirming that FDCA formation proceeds via DFF and FFCA as sequential intermediates during the oxidative transformation of HMF.

To identify the active oxygen species involved in the aerobic oxidation of HMF, a radical scavenger experiment was conducted under optimized reaction conditions. DMSO, a commonly used hydroxyl radical scavenger, was employed as the reaction medium to enhance FDCA yield. The high catalytic performance in the DMSO-water solvent system suggests that hydroxyl radicals do not participate in the reaction pathway. In contrast, the addition of *p*-benzoquinone, a superoxide radical (O_2^-) scavenger, led to a dramatic decrease in HMF conversion (6 %), strongly suggesting that O_2^- plays a crucial role in the catalytic process.

Kinetic studies on the transformation of HMF to FDCA were investigated with a Pd-Ru/S-CPOP catalyst. Based on the time-dependent reaction results (Fig. 10), the conversion of HMF to FDCA was divided into a three-step pathway model (Scheme S1), considering an irreversible one-way reaction. Reactions were conducted with different amounts of HMF under the optimized conditions (Fig. S11(a)), wherein Eq. (16) was used to calculate the rate constant (k_1; Fig. S11(b)) [31]. Subsequently, the logarithmic k_1 versus the logarithmic $[HMF]_0$ drew a graph of linear function (Fig. S11(c)), implying that the reaction follows first-order kinetics toward the HMF concentration. This result also implies that the transformations of DFF to FDCA via FFCA may also follow first-order kinetics. Using the k_1 value of the transformation of HMF to DFF, the rate constants for the subsequent oxidation steps (k_2 and k_3) could be derived by solving Eqs. (17)–(19). The resultant values for all steps in the oxidation process of HMF to FDCA are listed in Table 3. The rate constant for the conversion of FFCA to FDCA (k_3) was significantly lower than those for the other steps (k_1 and k_2), indicating that this step is the rate-determining step in the oxidation of HMF to FDCA over Pd-Ru/S-CPOP catalyst. In addition, the higher k_1 value than k_2 and k_3 values also suggest that oxidation of the hydroxyl group (–CH$_2$OH) to the aldehyde group (–CHO) is much easier than oxidation of the aldehyde group (–CHO) to the carboxylic acid group (–COOH), likely due to the greater accessibility of the HMF substrate to the Pd-Ru/S-CPOP catalyst, which agreed with previous reports [32,80].

$$\frac{d[HMF]}{dt} = -k_1[HMF] \tag{16}$$

$$\frac{d[DFF]}{dt} = k_1[HMF] - k_2[DFF] \tag{17}$$

$$\frac{d[FFCA]}{dt} = k_2[DFF] - k_3[FFCA] \tag{18}$$

$$\frac{d[FDCA]}{dt} = -k_3[FDCA] \tag{19}$$

$$\ln(k_i) = \ln(A) - \left(\frac{E_a}{RT}\right) \tag{20}$$

$$\ln\left(\frac{k_i}{T}\right) = \ln\left(\frac{k_B}{h}\right) + \frac{\Delta S^*}{R} - \frac{\Delta H^*}{RT} \tag{21}$$

$$\text{Gibbs free energy } (\Delta G^*) = -RT\ln\left(\frac{hk_i}{Tk_B}\right) \tag{22}$$

where k_i = rate constant (h^{-1}; i = 1, 2, and 3) for three consecutive oxidation steps of HMF oxidation to DFF (k_1), DFF oxidation to FFCA (k_2), and FFCA oxidation to FDCA (k_3).

The thermodynamic parameters for the oxidation of HMF to FDCA were also calculated using the Arrhenius Eq. (20), the linearized form of the Eyring Eq. (21), and Gibbs free energy Eq. (22) to find the feasibility of the reaction [76,77]. The activation energies for all the steps involved in the oxidation process were calculated from temperature-dependent kinetic experiments (Figs. 10, S12(a–c), and S13(a–b)), and their values are listed in Table 4. The smallest E_a value in the conversion of HMF to DFF revealed that oxidation of the hydroxyl group (–CH$_2$OH) to the aldehyde group (–CHO) is thermodynamically more feasible within this temperature range than the other steps. The ΔH^* and ΔS^* values were determined from the linear correlation plots (Figs. S12(d) and S13 (c–d)) of $\ln(k_i/T)$ vs $-1/RT$, where the slope and intercept values correspond to ΔH^* and $\left(\ln\left(\frac{k_B}{h}\right) + \frac{\Delta S^*}{R}\right)$, respectively. The ΔS^* value was then obtained by deriving the intercept (see pages S16–S17 in Supporting Information for calculation details). The positive value of ΔH^* (98.79 kJ mol^{-1}) for the conversion of FFCA to FDCA was much higher than for the other steps (Table 4), indicating the endothermic nature of the reaction and suggesting that a significant amount of external energy is required to form the catalyst–FFCA complex transition state [76,77]. Alternatively, ΔS^* values for every step are negative (Table 4), suggesting that the transition state of the reaction system is more ordered than the ground state, further confirming the non-spontaneous nature of the reaction [79]. The positive ΔG^* values for each step in the oxidation of HMF to FDCA at 130 °C also reinforce the non-spontaneous nature of the reaction (Table 4, also see page S18 in Supporting Information for calculation details). Finally, the catalytic performance of the Pd-Ru/S-CPOP catalyst in the base-free oxidation of HMF to FDCA was compared with previously reported solid catalysts (Table S4). This catalytic system attained a higher TOF (30.1 h^{-1}) without requiring base additives, likely due to its high surface area, synergistic effects between Pd and Ru NPs, and readily accessible active sites.

3.2.3. Direct conversion of fructose to FDCA via consecutive dehydration and aerobic oxidation processes

Based on the reaction studies above, the conversion of fructose to FDCA involves two reactions: (1) the dehydration of fructose to HMF and (2) the aerobic oxidation of HMF to FDCA. The former was catalyzed by sulfonic acid sites from S-CPOP that exhibited a high reaction rate and high HMF selectivity at 130 °C after 50 min. The latter reaction proceeded via Pd and Ru NPs under an O$_2$ atmosphere, achieving a high yield of FDCA at 130 °C after 6 h. Based on these findings, Pd-Ru/S-CPOP was investigated as a multifunctional catalyst for the direct synthesis of FDCA from fructose (Scheme 2).

As an initial experiment, we tested the Pd-Ru/S-CPOP catalyst (60 mg) in a pressurized reactor containing fructose (2 mmol), the molar ratio of fructose to Pd + Ru is 184:1 in DMSO:water (v/v; 3:2) solvent under 10 bar of O$_2$ at 130 °C for 8 h, resulting in a low FDCA yield of only 46 %. This low yield might be attributed to the undesired oxidation of fructose rather than the dehydration reaction, which generated undesired byproducts. To enhance the FDCA yield, the reaction was performed by a consecutive reaction method; O$_2$ was not purged during the first hour, expecting that fructose dehydration would occur more dominantly than the competitive oxidation reaction. Subsequently, the reactor was pressurized with O$_2$ (10 bar) for the remaining reaction time. This approach achieved a maximum FDCA yield of 95 %. To gain further insights into the reaction, the conversion of fructose to FDCA over the Pd-Ru/S-CPOP catalyst was monitored at various time intervals, as shown in Fig. 11(a). The data revealed that fructose rapidly produced 87 % HMF and 10 % DFF yield within the initial 1 h, wherein the fast production of HMF could be explained by the high k_{obs} value discussed above (Table 3). After purging with O$_2$ and extending the reaction time, the HMF yield gradually decreased while the yields of DFF and FFCA intermediates increased (reaction periods between 1 h to 3 h in Fig. 11(a)). With further increases in reaction time, the yields of these intermediates steadily diminished, and the FDCA yield increased to 95 % at 7 h. The photographic images of the reaction mixture before and after the reaction, as well as the reaction solution after catalyst separation, are shown in Fig. S14. To evaluate the potential applicability of this method, a gram-scale reaction was performed following the same experimental procedure using fructose (5 mmol), Pd-Ru/S-CPOP (150 mg), DMSO: water mixture (7.5:5.0 mL, v/v), and O$_2$ (25 bar) at 130 °C for 7 h. This reaction afforded FDCA in 80 % yield, which was moderately lower than that obtained in the small-scale condition, likely due to mass transfer limitations or differences in heat distribution at a larger scale. The performance of the multifunctional Pd-Ru/S-CPOP catalyst in the one-pot synthesis of FDCA from fructose was compared with previously reported catalytic systems (Table 5). In these reported catalytic systems, two different catalysts were used for the sequential conversion process: one catalyst facilitated the transformation of fructose to HMF, while a separate catalyst was employed for the oxidation of HMF to FDCA (see Table 5). However, these systems required external additives, resulting in low FDCA yields. In contrast, our catalytic system achieved a high FDCA yield without base additives or additional catalysts. This superior performance can be attributed to its high surface area, the abundance of the sulfonic acid group, the synergistic interaction between the Pd and Ru nanoparticle sites, and the presence of readily accessible active sites.

Based on our experimental findings and supported by literature precedents [14,23,31,42,81], a plausible mechanism was proposed for the one-pot reaction involving the dehydration of fructose to HMF, followed by its oxidation over Pd-Ru/S-CPOP in a DMSO:water solvent system (Scheme 5). The sulfonic acid moieties on the catalyst surface facilitate the dehydration of fructose. Due to the high solubility of fructose in the present solvent system, it readily diffuses into the catalyst, while DMSO serves as a proton transfer mediator between the catalyst and the fructose [14,23,42]. During dehydration, the hydroxyl group at the C2 position of fructose attacks the electrophilic sulfur atom of protonated DMSO. This attack simultaneously promotes proton transfer from the hydroxyl group to the oxygen atom of protonated DMSO, resulting in the elimination of the first water molecule and the formation of 3,4-dihydroxy-5-(hydroxymethyl)tetrahydrofuran-2-carbaldehyde intermediate. Subsequent dehydration steps involving the hydroxyl groups at the C3 and C4 positions are supported by the protonated DMSO. The elimination of two additional water molecules and the deprotonations facilitated by either the catalyst or DMSO, ultimately lead to the formation of HMF and regenerate the catalyst. In the oxidation of HMF, the O$_2$ was first activated by electron-rich Ru on the catalyst surface, generating O$_2^-$ species [31]. Kinetic studies (Fig. 10) reveal that the reaction proceeds via the formation of DFF as an intermediate. The hydroxyl group of HMF adsorbs onto the electron-deficient Pd surface (confirmed by XPS), forming a Pd-alkoxide complex. This undergoes β-hydride elimination to yield DFF along with the Pd-hydride species. The O$_2^-$ subsequently abstracts a proton from the Pd-hydride,
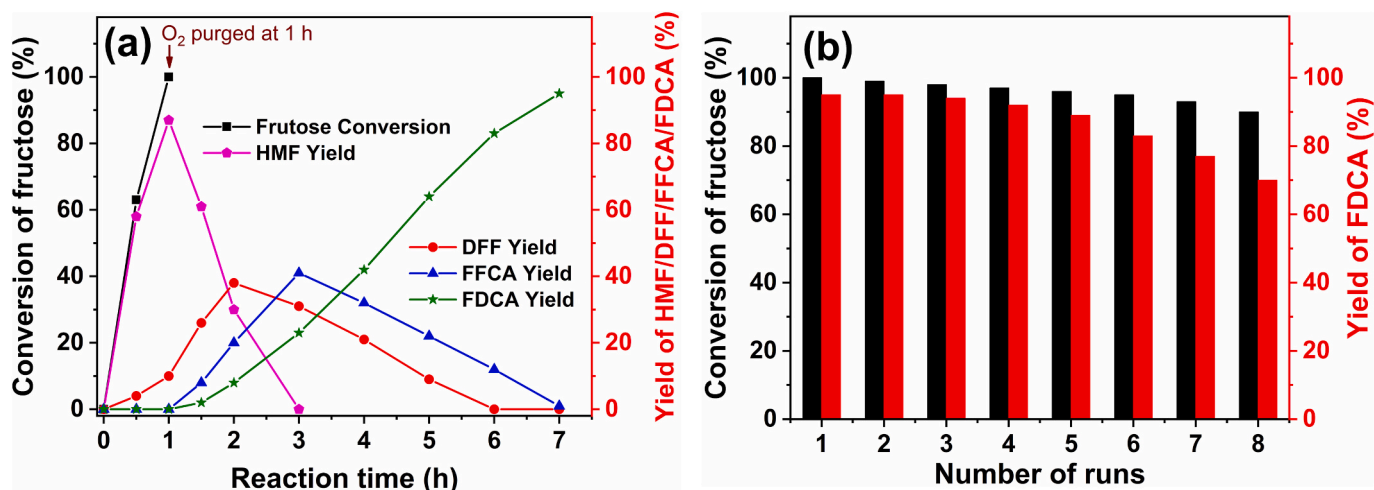
Fig. 11. (a) Time courses and (b) recycling studies of the Pd-Ru/S-CPOP catalyst for the direct synthesis of FDCA from fructose.

Table 5
Comparison of the present one-pot catalytic system with other reported methods.

Catalyst		Temp. (°C)	Oxidant	Time (h)	Additive	Process	FDCA Yield	Ref
Dehydration	Oxidation							
0.25 M HCl	Au/TiO$_2$	80	O$_2$	8	NaOH	Two-step	85	[44]
POP-SO$_3$H	Ru/MnO$_2$	110	O$_2$	12	–	Two-step	77	[45]
Amberlyst-15	Fe$_{0.6}$Zr$_{0.4}$O	160	O$_2$	24	[Bmim]Cl	One-pot	46	[46]
Amberlyst-15/CrCl$_3$.6 H$_2$O	Au-Pd/HT	95	O$_2$	50	Na$_2$CO$_3$	Triphasic/ Two-step	48	[47]
Fe$_3$O$_4$@SiO$_2$-SO$_3$H	Nano-Fe$_3$O$_4$-CoO$_x$	100	t-BuO$_2$H	15	–	Two-step	60	[48]
PBnNH$_3$C	Au/HT	140	O$_2$	10	Na$_2$CO$_3$	Two-step	74	[49]
Amberlyst-15	Pt/C	120	O$_2$	11	K$_2$CO$_3$	Two-step	88	[50]
Fe-zeolite	Mn-zeolite	150	O$_2$	5	pH 8 solution	One-pot	65	[51]
Pd-Ru/S-CPOP		130	O$_2$	7	–	One-pot	95	This work
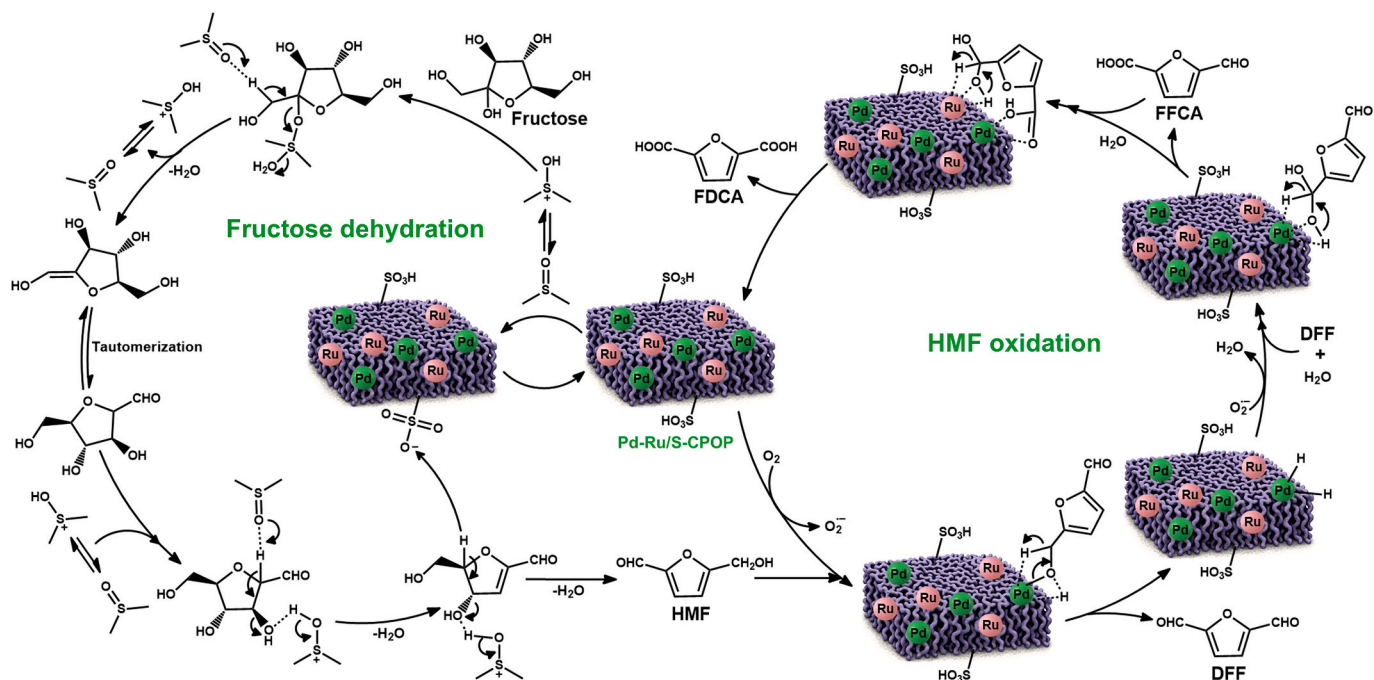
Scheme 5. Plausible mechanism for the conversion of fructose to FDCA over Pd-Ru/S-CPOP.

yielding water and regenerating the active Pd site. Following this, the water molecule attacks the aldehyde group of DFF, forming a diol intermediate, which then undergoes dehydrogenation to produce FFCA.

Some of the Pd exhibit a complex formation with the carboxylic acid moiety of FFCA due to their bidentate nature [82], which in turn inhibits the availability of active Pd sites for further oxidation of C5 aldehyde in

FFCA. To solve this issue, the adjacent Ru NPs facilitate the oxidation of FFCA to FDCA via a similar water-assisted attack and dehydrogenation pathway, owing to their relatively weaker interaction with carboxylic groups and strong dehydrogenation capabilities.

To confirm the cost-effectiveness and industrial viability of our catalyst, we evaluated the stability and reusability of the Pd-Ru/S-CPOP catalyst over eight repeated runs in the direct synthesis of FDCA from fructose under the optimized conditions [fructose (2 mmol), Pd-Ru/S-CPOP (60 mg), O_2 (10 bar), DMSO:water (v/v; 3:2), 130 °C, and 7 h] via a consecutive reaction method. After each reaction, the mixture was diluted with DMSO, and the catalyst was collected by centrifugation, washed thoroughly with DMSO and ethanol, dried at 160 °C for 2 h, and reused in subsequent runs. Fig. 11(b) displays that the catalytic conversion of fructose and the yield of FDCA remained largely consistent up to five runs. However, a moderate decrease in FDCA yield was observed from the sixth to the eighth run. This stable performance up to five runs can be attributed to the strong electronic interaction between the Pd-Ru NPs and the polymer support. The structural integrity of the Pd-Ru/S-CPOP catalyst after five runs was further examined using various analytical techniques (Fig. S15). FT-IR, powder XRD, and N_2 isotherm results (Fig. S15(a-c)) demonstrated that the reused catalyst exhibited no significant structural changes compared to the fresh one, and there were almost no guest molecules (reactants and products) inside the pores. FETEM image and particle size distribution histogram of the reused Pd-Ru/S-CPOP catalyst revealed that the Pd and Ru NPs had an average diameter of around 6 nm and were still evenly distributed on the S-CPOP surface (Fig. S15(d-e)). ICP–OES analysis of the filtrate solution from the fifth run confirmed no detectable leaching of Pd and Ru from the catalyst. The deconvoluted XPS of Pd and Ru for the catalyst after the fifth use showed an increased proportion of Pd(II) and Ru(IV) species compared to the fresh catalyst (Fig. 4 and Table S1), indicating surface oxidation during the reaction. The decline in FDCA yield observed after the fifth run (Fig. 11(b)) is likely attributed to the formation of more PdO and RuO_2, which may hinder both O_2 activation and the interaction between HMF and the active metallic sites. This inhibition could arise from electrostatic repulsion between HMF (and its intermediates) and the oxidized catalyst surface, ultimately reducing the efficiency of HMF oxidation and leading to a lower FDCA yield [33,81]. A slight decrease in the binding energy shift difference was also observed in the used catalyst compared to the fresh one (see Fig. 4 and Table S2), indicating a diminished degree of electron transfer from Pd to Ru. This attenuation in electron transfer likely suppresses the formation of reactive O_2^- species, thereby decreasing the efficiency of the oxidation process. The amounts of Brønsted and Lewis acids in the reused Pd-Ru/S-CPOP catalyst were estimated to be 1.08 mmol g^{-1} and 3.04 mmol g^{-1}, respectively, based on the FT-IR spectrum of the pyridine-adsorbed recovered catalyst (Fig. S1(b)). A slight decrease in Lewis acidity was observed compared to the fresh catalyst, suggesting a minor loss of Pd and/or Ru NPs from the support during the catalytic cycle. These results demonstrate that the Pd-Ru/S-CPOP catalyst maintains its structural stability, nanoparticle dispersion, and catalytic activity across multiple runs, making it a highly robust and effective catalyst for the biomass-derived conversion of fructose to FDCA. This combination of high reusability, stability, and efficiency positions the Pd-Ru/S-CPOP catalyst as a promising candidate for industrial applications in the sustainable production of bio-based chemicals.

4. Conclusions

In this study, a sulfonic acid-functionalized porous organic polymer (S-CPOP) was successfully synthesized using an economically viable and straightforward method, offering a high surface area, mesoporosity, and abundant acid sites. The S-CPOP catalyst exhibited excellent performance in the fructose dehydration to HMF at 130 °C, due to the presence of sulfonic acid functionalities integrated into the polymer network. The S-CPOP was also employed as a support for monometallic (Pd or Ru) and bimetallic (Pd-Ru) nanoparticles (NPs). The resulting Pd-Ru/S-CPOP catalyst showed remarkable efficiency in the base-free aerobic oxidation of HMF to FDCA, outperforming both the monometallic Pd and Ru catalysts. Optimization of reaction parameters and kinetic analysis revealed that the oxidation process of HMF to FDCA proceeded via DFF and FFCA as intermediate species. Rate constants and thermodynamic parameters for each step in the reaction were determined, and it was found that the conversion of FFCA to FDCA is the rate-determining step in the oxidation process over the Pd-Ru/S-CPOP catalyst. Furthermore, the direct, one-pot synthesis of FDCA from fructose was successfully achieved with the Pd-Ru/S-CPOP catalyst, yielding 95 % FDCA. The superior catalytic activity of the bimetallic catalyst can be attributed to several factors: (i) mesoporous structure accessing the efficient mass transfer and reactant accessibility; (ii) the abundant sulfonic acid groups facilitating the fructose dehydration process; and (iii) the synergistic effects of Pd and Ru NPs, combined with the high content of heteroatoms in the catalyst, significantly facilitated the activation of O_2, thereby accelerating the subsequent HMF oxidation process. Importantly, the Pd-Ru/S-CPOP catalyst exhibited superior stability and reusability, maintaining high activity over five consecutive reaction runs without significant structural degradation or metal leaching. The facile synthesis, high catalytic efficiency, and sustainable reaction conditions make the proposed catalytic system a promising candidate for industrial applications in biomass valorization. By enabling a cost-effective, environmentally friendly, and base-free route to FDCA production from biomass-derived fructose, this study contributes to the advancement of green chemistry and the development of bio-based alternatives to petroleum-derived polymers.

CRediT authorship contribution statement

Pillaiyar Puthiaraj: Writing – original draft, Methodology, Conceptualization. **Jongmin Park:** Methodology, Formal analysis. **Yuyeol Choi:** Investigation, Data curation. **Woosung Leem:** Formal analysis, Data curation. **Kyungsu Na:** Writing – review & editing, Validation, Supervision, Resources.

Declaration of competing interest

The authors declare that they have no known competing financial interests or personal relationships that could have appeared to influence the work reported in this paper.

Acknowledgments

Appendix A. Supplementary data

Supplementary data to this article can be found online at https://doi.org/10.1016/j.cej.2025.167222.

Data availability

Data will be made available on request.

References

[1] S. Kar, Q.-Q. Zhou, Y. Ben-David, D. Milstein, Catalytic furfural/5-hydroxymethyl furfural oxidation to furoic acid/furan-2,5-dicarboxylic acid with H_2 production using alkaline water as the formal oxidant, J. Am. Chem. Soc. 144 (2022) 1288–1295.

[2] X. Shi, X. Xing, M. Ruan, Q. Wei, Y. Guan, H. Gao, S. Xu, Efficient conversion of cellulose into 5-hydroxymethylfurfural by inexpensive SO_4^{2-}/HfO$_2$ catalyst in a green water-tetrahydrofuran monophasic system, Chem. Eng. J. 472 (2023) 145001.

[3] T. Shen, L. Hou, J. Gosset, H. Wang, S. Leng, Y. Boumghar, S. Barghi, C. Xu, Recent advances in processes and technologies for production of 5-hydroxymethylfurfural and 2,5-furandicarboylic acid from carbohydrates, Chem. Eng. J. 500 (2024) 156470.

[4] A.F. Sousa, C. Vilela, A.C. Fonseca, M. Matos, C.S.R. Freire, G.-J.M. Gruter, J.F. J. Coelho, A.J.D. Silvestre, Biobased polyesters and other polymers from 2,5-fur-andicarboxylic acid: a tribute to furan excellency, Polym. Chem. 6 (2015) 5961–5983.

[5] D.I. Collias, A.M. Harris, V. Nagpal, I.W. Cottrell, M.W. Schultheis, Biobased terephthalic acid technologies: a literature review, Ind. Biotechnol. 10 (2014) 91–105.

[6] F.H. Isikgor, C.R. Becer, Lignocellulosic biomass: a sustainable platform for the production of bio-based chemicals and polymers, Polym. Chem. 6 (2015) 4497–4559.

[7] B. Liu, Z. Zhang, Catalytic conversion of biomass into chemicals and fuels over magnetic catalysts, ACS Catal. 6 (2016) 326–338.

[8] L. Qi, Y.F. Mui, S.W. Lo, M.Y. Lui, G.R. Akien, I.T. Horváth, Catalytic conversion of fructose, glucose, and sucrose to 5-(hydroxymethyl)furfural and levulinic and formic acids in γ-valerolactone as a green solvent, ACS Catal. 4 (2014) 1470–1477.

[9] Q. Ren, Y. Huang, H. Ma, J. Gao, J. Xu, Catalytic conversion of carbohydrates to 5-hydroxymethylfurfural promoted by metal halides, Chin. J. Catal. 35 (2014) 496–500.

[10] B. Cai, R. Kang, D. Guo, J. Feng, T. Ma, H. Pan, An eco-friendly acidic catalyst phosphorus-doped graphitic carbon nitride for efficient conversion of fructose to 5-hydroxymethylfurfural, Renew. Energy 199 (2022) 1629–1638.

[11] T. Chhabra, A. Bahuguna, S.S. Dhankhar, C.M. Nagaraja, V. Krishnan, Sulfonated graphitic carbon nitride as a highly selective and efficient heterogeneous catalyst for the conversion of biomass-derived saccharides to 5-hydroxymethylfurfural in green solvents, Green Chem. 21 (2019) 6012–6026.

[12] C. Tempelman, U. Jacobs, J. Herselman, R. van Driel, F. Schraa, J. Versijde, T. van Waversveld, Y. Yagci, M. Barg, F. Smits, K. Kuijpers, K. Lamers, T. Remijn, V. Degirmenci, Waste apple biomass conversion to 5-HMF over tin doped sulfonated activated carbon as a catalyst, Biomass Bioenergy 168 (2023) 106661.

[13] M. Li, L. Huai, Y. Zhang, H. Ma, P. Zhang, F. Xu, J. Zhang, L. Jiang, A binary catalytic system of sulfonated metal–organic frameworks and deep eutectic solvents towards highly efficient synthesis of 5-hydroxymethylfurfural from fructose, Chem. Eng. J. 493 (2024) 152767.

[14] S. Darvishi, S. Sadjadi, E. Monflier, A. Heydari, M.M. Heravi, Sulfonic acid-functionalized k-carrageenan/Cr-based metal-organic framework: An efficient and recyclable catalyst for fructose conversion to 5-hydroxymethylfurfural, Int. J. Biol. Macromol. 264 (2024) 130555.

[15] F.J. Morales-Leal, J. Rivera de la Rosa, C.J. Lucio-Ortiz, D.A. De Haro-Del Rio, C. Solis Maldonado, S. Wi, L.B. Casabianca, C.D. Garcia, Dehydration of fructose over thiol– and sulfonic– modified alumina in a continuous reactor for 5-HMF production: study of catalyst stability by NMR, Appl. Catal. Environ. 244 (2019) 250–261.

[16] J. Pang, J. Sun, M. Zheng, H. Li, Y. Wang, T. Zhang, Transition metal carbide catalysts for biomass conversion: a review, Appl. Catal. Environ. 254 (2019) 510–522.

[17] V. Arumugam, P. Sriram, T.-J. Yen, G.G. Redhi, R.M. Gengan, Nano-material as an excellent catalyst for reducing a series of nitroanilines and dyes: triphosphonated ionic liquid- CuFe$_2$O$_4$-modified boron nitride, Appl. Catal. Environ. 222 (2018) 99–114.

[18] Q. Hou, M. Zhen, W. Li, L. Liu, J. Liu, S. Zhang, Y. Nie, C. Bai, X. Bai, M. Ju, Efficient catalytic conversion of glucose into 5-hydroxymethylfurfural by aluminum oxide in ionic liquid, Appl. Catal. Environ. 253 (2019) 1–10.

[19] S. Khoonsap, L. Buengkitcharoen, S. Amnuaypanich, N. Thongnoppakhun, N. Patdhanagul, S. Suthirakun, C. Sukpattanacharoen, S. Amnuaypanich, Synergistic effect of silanols in mesopores leading to unexpected catalysis of dendritic mesoporous silica particles in the aqueous-phase synthesis of 5-hydrox-ymethylfurfural from fructose, Chem. Eng. J. 477 (2023) 147074.

[20] Z. Yang, W. Qi, R. Huang, J. Fang, R. Su, Z. He, Functionalized silica nanoparticles for conversion of fructose to 5-hydroxymethylfurfural, Chem. Eng. J. 296 (2016) 209–216.

[21] X. Yang, M.M. Sadughi, A. Bahadoran, M. Al-Haideri, P. Ghamari Kargar, A. S. Noori, S.M. Sajjadinezhad, A new method for conversion of fructose and glucose to 5-hydroxymethylfurfural by magnetic mesoporous of SBA-16 was modified to sulfonic acid as Lewis's acid catalysts, Renew. Energy 209 (2023) 145–156.

[22] M. Niakan, P. Ghamari Kargar, B. Maleki, R.S. Zabibah, M. Daryapeima, S. Sedigh Ashrafi, S. Zhou, Ternary AgFe$_2$O$_4$/SBA-16/SO$_3$H heterojunction photocatalyst for the sustainable production of 5-hydroxymethylfurfural under mild conditions, Langmuir 41 (2025) 13220–13232.

[23] H. Hafizi, A. Najafi Chermahini, M. Saraji, G. Mohammadnezhad, The catalytic conversion of fructose into 5-hydroxymethylfurfural over acid-functionalized KIT-6, an ordered mesoporous silica, Chem. Eng. J. 294 (2016) 380–388.

[24] Y. Shi, Z. Zhou, T. Tana, C. Su, H.Y. Zhu, A.C. Bissember, J. Huang, P. Han, S. Sarina, Photoactive single-site Tin(IV) catalyst for 5-hydroxymethylfurfural production from sugars, ACS Catal. 15 (2025) 2950–2958.

[25] P.G. Kargar, M. Niakan, B. Maleki, R.S. Zabibah, M.A. Apoorvari, S.S. Ashrafi, S. Arghavani, S. Zhou, Heterogeneous photocatalytic conversion of biomass-derived sugars into 5-hydroxymethylfurfural over AgFe$_2$O$_4$/TiO$_2$–SO$_3$H nanocomposite, ACS Sustain. Chem. Eng. 12 (2024) 18149–18160.

[26] L. Ardemani, G. Cibin, A.J. Dent, M.A. Isaacs, G. Kyriakou, A.F. Lee, C.M.A. Parlett, S.A. Parry, K. Wilson, Solid base catalysed 5-HMF oxidation to 2,5-FDCA over Au/hydrotalcites: fact or fiction? Chem. Sci. 6 (2015) 4940–4945.

[27] D.K. Mishra, J.K. Cho, Y. Yi, H.J. Lee, Y.J. Kim, Hydroxyapatite supported gold nanocatalyst for base-free oxidative esterification of 5-hydroxymethyl-2-furfural to 2,5-furan dimethylcarboxylate with air as oxidant, J. Ind. Eng. Chem. 70 (2019) 338–345.

[28] B. Siyo, M. Schneider, M.-M. Pohl, P. Langer, N. Steinfeldt, Synthesis, characterization, and application of PVP-Pd NP in the aerobic oxidation of 5-hydroxymethylfurfural (HMF), Catal. Lett. 144 (2014) 498–506.

[29] F. Liguori, P. Barbaro, N. Calisi, Continuous-flow oxidation of HMF to FDCA by resin-supported platinum catalysts in neat water, ChemSusChem 12 (2019) 2558–2563.

[30] H. Yu, K.-A. Kim, M.J. Kang, S.Y. Hwang, H.G. Cha, Carbon support with tunable porosity prepared by carbonizing chitosan for catalytic oxidation of 5-hydroxylmethylfurfural, ACS Sustain. Chem. Eng. 7 (2019) 3742–3748.

[31] J. Zhang, P. Chen, H. Liu, R. Zhang, W. Jia, J. Zhang, L. Peng, Electron-rich ruthenium nanoparticles on nitrogen-doped carbon for the efficient catalytic oxidation of 5-hydroxymethylfurfural into 2,5-furandicarboxylic acid, Appl. Catal. Gen. 676 (2024) 119663.

[32] C.M. Pichler, M.G. Al-Shaal, D. Gu, H. Joshi, W. Ciptonugroho, F. Schüth, Ruthenium supported on high-surface-area zirconia as an efficient catalyst for the base-free oxidation of 5-hydroxymethylfurfural to 2,5-furandicarboxylic acid, ChemSusChem 11 (2018) 2083–2090.

[33] G. Yi, S.P. Teong, Y. Zhang, Base-free conversion of 5-hydroxymethylfurfural to 2,5-furandicarboxylic acid over a Ru/C catalyst, Green Chem. 18 (2016) 979–983.

[34] T. Gao, J. Chen, W. Fang, Q. Cao, W. Su, F. Dumeignil, Ru/MnXCe1OY catalysts with enhanced oxygen mobility and strong metal-support interaction: exceptional performances in 5-hydroxymethylfurfural base-free aerobic oxidation, J. Catal. 368 (2018) 53–68.

[35] H. Xia, J. An, M. Hong, S. Xu, L. Zhang, S. Zuo, Aerobic oxidation of 5-hydroxy-methylfurfural to 2,5-difurancarboxylic acid over Pd-au nanoparticles supported on Mg-Al hydrotalcite, Catal. Today 319 (2019) 113–120.

[36] X. Wan, C. Zhou, J. Chen, W. Deng, Q. Zhang, Y. Yang, Y. Wang, Base-free aerobic oxidation of 5-hydroxymethyl-furfural to 2,5-furandicarboxylic acid in water catalyzed by functionalized carbon nanotube-supported Au–Pd alloy nanoparticles, ACS Catal. 4 (2014) 2175–2185.

[37] Z. Gao, R. Xie, G. Fan, L. Yang, F. Li, Highly efficient and stable bimetallic AuPd over La-doped Ca–Mg–Al layered double hydroxide for base-free aerobic oxidation of 5-hydroxymethylfurfural in water, ACS Sustain. Chem. Eng. 5 (2017) 5852–5861.

[38] Z. Zhang, J. Jia, Y. Zhi, S. Ma, X. Liu, Porous organic polymers for light-driven organic transformations, Chem. Soc. Rev. 51 (2022) 2444–2490.

[39] P. Puthiaraj, S. Ravi, K. Yu, W.-S. Ahn, CO$_2$ adsorption and conversion into cyclic carbonates over a porous ZnBr$_2$-grafted N-heterocyclic carbene-based aromatic polymer, Appl. Catal. Environ. 251 (2019) 195–205.

[40] R. Iqbal, G. Yasin, M. Hamza, S. Ibraheem, B. Ullah, A. Saleem, S. Ali, S. Hussain, T. Anh Nguyen, Y. Slimani, R. Pathak, State of the art two-dimensional covalent organic frameworks: prospects from rational design and reactions to applications for advanced energy storage technologies, Coord. Chem. Rev. 447 (2021) 214152.

[41] S. Ge, K. Wei, W. Peng, R. Huang, E. Akinlabi, H. Xia, M.W. Shahzad, X. Zhang, B. B. Xu, J. Jiang, A comprehensive review of covalent organic frameworks (COFs) and their derivatives in environmental pollution control, Chem. Soc. Rev. 53 (2024) 11259–11302.

[42] S. Ravi, Y. Choi, J.K. Choe, Achieving effective fructose-to-5-hydroxymethylfurfural conversion via facile synthesis of large surface phosphate-functionalized porous organic polymers, Appl. Catal. Environ. 271 (2020) 118942.

[43] J. Artz, R. Palkovits, Base-free aqueous-phase oxidation of 5-hydroxymethylfurfu-ral over ruthenium catalysts supported on covalent triazine frameworks, ChemSusChem 8 (2015) 3832–3838.

[44] P. Rapado, C. Lois, M. Cano, L. Faba, S. Ordóñez, Biomass to plastics: from HMF to fructose for the synthesis of 2,5-furandicarboxylic acid over Au/TiO$_2$, Catal. Today 445 (2025) 115036.

[45] P. Manjunathan, B.S. Rao, M. Lee, M.J. Hidajat, G.-N. Yun, D.W. Hwang, Integrated process towards sustainable renewable plastics: production of 2,5-furandicarbox-ylic acid from fructose in a base-free environment, Appl. Catal. Gen. 667 (2023) 119446.

[46] D. Yan, G. Wang, K. Gao, X. Lu, J. Xin, S. Zhang, One-pot synthesis of 2,5-furan-dicarboxylic acid from fructose in ionic liquids, Ind. Eng. Chem. Res. 57 (2018) 1851–1858.

[47] G. Yi, S.P. Teong, Y. Zhang, The direct conversion of sugars into 2,5-furandicar-boxylic acid in a triphasic system, ChemSusChem 8 (2015) 1151–1155.

[48] S. Wang, Z. Zhang, B. Liu, Catalytic conversion of fructose and 5-hydroxymethyl-furfural into 2,5-furandicarboxylic acid over a recyclable Fe$_3$O$_4$–CoOx magnetite nanocatalyst, ACS Sustain. Chem. Eng. 3 (2015) 406–412.

[49] S.P. Teong, G. Yi, X. Cao, Y. Zhang, Poly-benzylic ammonium chloride resins as solid catalysts for fructose dehydration, ChemSusChem 7 (2014) 2120–2124.

[50] G. Chen, L. Wu, H. Fan, B.-G. Li, Highly efficient two-step synthesis of 2,5-furan-dicarboxylic acid from fructose without 5-hydroxymethylfurfural (hmf) separation: in situ oxidation of hmf in alkaline aqueous H$_2$O/DMSO mixed solvent under mild conditions, Ind. Eng. Chem. Res. 57 (2018) 16172–16181.

[51] N.V. Fathima Safeeda, M. Balachandran, U.B.R. Ragula, Engineering a heterogeneous catalyst with earth-abundant metal oxides for efficient one-pot synthesis of 2,5-furan dicarboxylic acid from agro-waste, J. Environ. Chem. Eng. 13 (2025) 115653.

[52] M. Li, L. Jiang, S. Feng, J. Huang, P. Zhang, J. Zhang, Aluminum ion intercalation in mesoporous multilayer carbocatalysts promotes the conversion of glucose to 5-hydroxymethylfurfural, Dalton Trans. 53 (2024) 3386–3396.

[53] Y. Feng, H. Liu, W. Luo, E. Liu, N. Zhao, K. Yoshino, W. Feng, Covalent functionalization of graphene by azobenzene with molecular hydrogen bonds for long-term solar thermal storage, Sci. Rep. 3 (2013) 3260.

[54] Q.T. Trinh, K. Bhola, P.N. Amaniampong, F. Jérôme, S.H. Mushrif, Synergistic application of XPS and DFT to investigate metal oxide surface catalysis, J. Phys. Chem. C 122 (2018) 22397–22406.

[55] J. Kim, S. Ravi, K. Kim, Y. Choi, H.-H. Park, Y.-S. Bae, Novel porous organic polymer catalyst with phosphate and sulfonic acid sites for facile esterification of levulinic acid, ACS Appl. Mater. Interfaces 15 (2023) 48485–48494.

[56] W. Pang, J. Xue, H. Pang, A high energy density azobenzene/graphene oxide hybrid with weak nonbonding interactions for solar thermal storage, Sci. Rep. 9 (2019) 5224.

[57] W.-R. Cai, W.-K. Zhu, B.-Z. Yang, D.-T. Wu, J.-Y. Li, Z.-Z. Yin, Y. Kong, Porphyrin-based metal–organic frameworks for efficient electrochemiluminescent chiral recognition of tyrosine enantiomers, Chemosensors 10 (2022) 519.

[58] A.S. Rocha, A.M.S. Forrester, M.H.C. de la Cruz, C.T. da Silva, E.R. Lachter, Comparative performance of niobium phosphates in liquid phase anisole benzylation with benzyl alcohol, Catal. Commun. 9 (2008) 1959–1965.

[59] G. Liu, Y. Wang, C. Shen, Z. Ju, D. Yuan, A facile synthesis of microporous organic polymers for efficient gas storage and separation, J Mater Chem A 3 (2015) 3051–3058.

[60] Z. Liu, C. Wang, P. Yang, W. Wang, H. Gao, G. An, S. Liu, J. Chen, T. Guo, X. Xu, G. Wang, Microenvironment and electronic state modulation of Pd nanoparticles within MOFs for enhancing low-temperature activity towards DCPD hydrogenation, Chin. J. Catal. 64 (2024) 112–122.

[61] X. Zhang, L. Xia, G. Zhao, B. Zhang, Y. Chen, J. Chen, M. Gao, Y. Jiang, Y. Liu, H. Pan, W. Sun, Fast and durable alkaline hydrogen oxidation reaction at the electron-deficient ruthenium–ruthenium oxide interface, Adv. Mater. 35 (2023) 2208821.

[62] K. Vinokurov, Y. Bekenstein, V. Gutkin, I. Popov, O. Millo, U. Banin, Rhodium growth on Cu$_2$S nanocrystals yielding hybrid nanoscale inorganic cages and their synergistic properties, CrystEngComm 16 (2014) 9506–9512.

[63] Z. Li, J. Jiang, Y. Hu, Electron transfer between Pd–Ru nanoalloys supported on CeO$_2$ promotes co-catalytic oxidation, Langmuir 41 (2025) 16235–16242.

[64] Y. Liu, X. Hu, C. Liu, S. Zhu, K. Jiang, F. Liu, S. Zheng, Construction of Pd-doped RuO$_2$ nanosheets for efficient and stable acidic water oxidation, Green Energy Environ. 9 (2024) 937–948.

[65] R.A. Dar, L. Giri, S.P. Karna, A.K. Srivastava, Performance of palladium nanoparticle–graphene composite as an efficient electrode material for electrochemical double layer capacitors, Electrochim. Acta 196 (2016) 547–557.

[66] J. Mondal, S.K. Kundu, W.K. Hung Ng, R. Singuru, P. Borah, H. Hirao, Y. Zhao, A. Bhaumik, Fabrication of ruthenium nanoparticles in porous organic polymers: towards advanced heterogeneous catalytic nanoreactors, Chem. A Eur. J. 21 (2015) 19016–19027.

[67] K. Kusada, H. Kobayashi, R. Ikeda, Y. Kubota, M. Takata, S. Toh, T. Yamamoto, S. Matsumura, N. Sumi, K. Sato, K. Nagaoka, H. Kitagawa, Solid solution alloy nanoparticles of immiscible Pd and Ru elements neighboring on Rh: changeover of the thermodynamic behavior for hydrogen storage and enhanced CO-oxidizing ability, J. Am. Chem. Soc. 136 (2014) 1864–1871.

[68] S. Belfqueh, A. Seron, S. Chapron, G. Arrachart, N. Menad, Evaluating organic acids as alternative leaching reagents for rare earth elements recovery from NdFeB magnets, J. Rare Earths 41 (2023) 621–631.

[69] X. Song, Y. Liao, T. Liu, D. Yin, H. Wang, L. Chen, L. Ma, H. Yang, L. G. Voskressensky, C. Wang, A highly effective approach to enhance the performance of biomass-derived acid for fructose conversion to 5-hydroxymethylfurfural, Fuel Process. Technol. 234 (2022) 107318.

[70] X. Qi, H. Guo, L. Li, R.L. Smith Jr., Acid-catalyzed dehydration of fructose into 5-hydroxymethylfurfural by cellulose-derived amorphous carbon, ChemSusChem 5 (2012) 2215–2220.

[71] G. Tsilomelekis, T.R. Josephson, V. Nikolakis, S. Caratzoulas, Origin of 5-hydroxymethylfurfural stability in water/dimethyl sulfoxide mixtures, ChemSusChem 7 (2014) 117–126.

[72] L. Shuai, J. Luterbacher, Organic solvent effects in biomass conversion reactions, ChemSusChem 9 (2016) 133–155.

[73] P. Körner, D. Jung, A. Kruse, The effect of different Brønsted acids on the hydrothermal conversion of fructose to HMF, Green Chem. 20 (2018) 2231–2241.

[74] P. Cao, Y. Li, Y. Li, X. Zhang, X. Wang, Z. Jiang, Surfactant decorated hydrotalcite-supported polyoxometalates for aerobic oxidation of 5-hydroxymethylfurfural and monosaccharides, Sustain. Energy Fuel 4 (2020) 2236–2248.

[75] X. Cheng, S. Li, S. Liu, Y. Xin, J. Yang, B. Chen, H. Liu, Highly efficient catalytic oxidation of 5-hydroxymethylfurfural to 2,5-furandicarboxylic acid using bimetallic Pt–Cu alloy nanoparticles as catalysts, Chem. Commun. 58 (2022) 1183–1186.

[76] R. Tomer, P. Biswas, Reaction kinetics study and the estimation of thermodynamic parameters for the conversion of glucose to 5-hydroxymethylfurfural (5-HMF) in a dimethyl sulfoxide (DMSO) medium in the presence of a mesoporous TiO$_2$ catalyst, J. Taiwan Inst. Chem. Eng. 136 (2022) 104427.

[77] S. Mahala, S.M. Arumugam, R.K. Kunchala, B. Devi, S. Elumalai, A mesoporous Ta$_2$O$_5$/Nb$_2$O$_5$ nanocomposite with Lewis/Brønsted acid sites to enhance stepwise glucose conversion to 5-hydroxymethylfurfural, Sustain. Energy Fuel 8 (2024) 2219–2234.

[78] K.C. Badgujar, B.M. Bhanage, Thermo-chemical energy assessment for production of energy-rich fuel additive compounds by using levulinic acid and immobilized lipase, Fuel Process. Technol. 138 (2015) 139–146.

[79] L.K. Ong, A. Kurniawan, A.C. Suwandi, C.X. Lin, X.S. Zhao, S. Ismadji, Transesterification of leather tanning waste to biodiesel at supercritical condition: kinetics and thermodynamics studies, J. Supercrit. Fluids 75 (2013) 11–20.

[80] A.B. Gawade, A.V. Nakhate, G.D. Yadav, Selective synthesis of 2, 5-furandicarboxylic acid by oxidation of 5-hydroxymethylfurfural over MnFe$_2$O$_4$ catalyst, Catal. Today 309 (2018) 119–125.

[81] T. Gao, Y. Yin, W. Fang, Q. Cao, Highly dispersed ruthenium nanoparticles on hydroxyapatite as selective and reusable catalyst for aerobic oxidation of 5-hydroxymethylfurfural to 2,5-furandicarboxylic acid under base-free conditions, Mol. Catal. 450 (2018) 55–64.

[82] I.A. Efimenko, N.A. Ivanova, O.S. Erofeeva, N.N. Efimov, L.I. Demina, A.A. Averin, N.P. Simonenko, Effect of the position of double bonds of unsaturated carboxylic acids on the type of the resulting palladium(I) coordination polymers, Russ. J. Inorg. Chem. 70 (2025) 34–41.